ANL-81-11

ANL-81-11

MATERIALS TECHNOLOGY FOR COAL-CONVERSION PROCESSES

Progress Report for October—December 1980

ARGONNE NATIONAL LABORATORY, ARGONNE, ILLINOIS

Prepared for the Office of Fossil Energy
U. S. DEPARTMENT OF ENERGY
under Contract W-31-109-Eng-38

TABLE OF CONTENTS

LIST OF FIGURES

LIST OF FIGURES (continued)

LIST OF TABLES

MATERIALS TECHNOLOGY FOR COAL-CONVERSION PROCESSES
Progress Report for
October-December 1980

HIGHLIGHTS

Task A - Evaluation of Ceramic Refractories for Slagging Gasifiers *(C.R. Kennedy, R.J. Fousek, and S.W. Kreis)*

Cores taken from the slag-refractory interface of seven of the refractories exposed to a high-iron oxide acidic coal slag (base-to-acid ratio = 0.5) in test run 12 have been examined using reflected light microscopy, scanning electron microscopy with energy dispersive x-ray analysis, and x-ray diffraction. Electron microprobe analysis is in progress. The results indicate that the alumina-chromia refractories react with the slag to form complex $(Mg,Fe)(Al,Cr)_2O_4$-type spinels that vary in composition, coherentness, and thickness depending on the composition and density of the original refractory. Significant amounts of intergranular attack were also observed in the non-fused-cast refractories, especially those with chemical bonding.

Task B - Development and Application of Nondestructive Evaluation Methods for Coal-conversion Processes *(W.A. Ellingson, C.A. Youngdahl, K.J. Reimann, and M.J. Caines)*

Results of automated erosion scanning of a hardfaced carbon steel tar-separator cyclone at the Morgantown Energy Technology Center Fixed-bed Gasifier were compared with those obtained by manual ultrasonic surveying. The erosive wear for a two-week operating period was less than 0.25 mm in the inlet zone, and the erosion scanner data agreed well with the data obtained manually. The HYCAS high-pressure cyclone separator was radiographically inspected for additional wear and some areas of the cyclone internals were found to have worn through. An automated erosion monitoring system using pressure-coupled waveguides was designed and partially installed at the Exxon Coal Liquefaction Plant in Baytown, TX. The installation will be completed by the next reporting period. Additional waveguides and electronic switching equipment were installed in the ANL erosion scanning system at the Solvent Refined Coal liquefaction plant in Ft. Lewis, WA, and the system was interconnected to the plant computer. After compensation for temperature, the measurement error is within ± 0.05 mm. Development of a 1.2-m-long bimetallic tapered waveguide for installation in March 1981 is continuing.

The literature on the state of the art of electromagnetic acoustic transducers (EMATs) was reviewed to assess the feasibility of applying a high-temperature version of such a transducer to automatic erosion monitoring. The advantage of EMATs is that they do not require surface attachment, and therefore afford considerable flexibility in obtaining erosive wear profiles. A shear-wave EMAT was procured and some preliminary evaluation tests conducted. While the system performs adequately on aluminum, problems were encountered when testing stainless steel, necessitating additional efforts before field testing is feasible.

Task C - Corrosion Behavior of Materials in Coal-conversion Processes
(K. Natesan)

A number of experiments have been conducted to establish the mechanism(s) of sulfidation and breakaway corrosion behavior of materials exposed to complex gas environments. The alloys selected for the investigation are Incoloy 800, Inconel 671, Type 310 stainless steel, RA 333, GE 1541, and pure metals such as chromium and iron. Preliminary results are reported for chromium and Incoloy 800 specimens that were preoxidized in low-oxygen atmospheres and subsequently sulfidized in oxygen-free atmospheres.

Task D - Failure Analysis *(D.R. Diercks, G.L. Fogle, and G.M. Dragel)*

Two of four experimental thermowells that were exposed for six runs in the U-Gas Pilot Plant were found to have suffered significant degradation, and these two components have been examined metallographically and in the SEM. The first of these, fabricated of uncoated Haynes 188, suffered substantial erosive wear at the tip, and oxidation and sulfide formation were present both near and away from the region of greatest erosive wear. The second thermowell, made of aluminized Type 310 stainless steel, also showed extensive erosion and corrosive attack at the tip. At other locations, the aluminized coating was generally intact and protective.

The failure analysis of a sample of product gas piping from the BiGas Pilot Plant has been completed. The failure was attributed to polythionic acid-induced intergranular stress-corrosion cracking.

MATERIALS TECHNOLOGY FOR COAL-CONVERSION PROCESSES
Progress Report for
October-December 1980

FOREWORD

This materials engineering program, begun in 1974, includes studies on ceramic (refractory) and metallic materials presently being used or intended for use in coal conversion processes. The program entails efforts in nondestructive testing and failure analysis, as well as studies of erosive wear, corrosion, and refractory degradation. Appropriate laboratory and field experiments are integrated such that the results have impact on present pilot- and demonstration-plant and proposed full-scale designs. This report presents the technical accomplishments of the program for the period October-December 1980.

ABSTRACT

An examination of cores taken from the slag-refractory interface of seven refractories exposed to high-iron oxide acidic coal slags indicates the formation of complex $(Mg,Fe)(Al,Cr)_2O_4$-type spinels with characteristics that vary with the composition and density of the original refractory. Significant amounts of intergranular attack were also observed in the non-fused-cast refractories, especially those with chemical bonding.

The results of automated erosion scanning system measurements on a tar-separator cyclone at the Morgantown Energy Technology Center Stirred-bed/Fixed-bed Gasifier are reported, as are measurements on the HYGAS high-pressure cyclone. Installation of an automated erosion monitoring system using pressure-coupled waveguides is under way at the Exxon Coal Liquefaction Plant in Baytown, TX, and additional waveguides and switching equipment have been installed at the Solvent Refined Coal liquefaction plant in Ft. Lewis, WA. The literature on the state of the art of electromagnetic acoustic transducers (EMATs) was reviewed to assess their possible use in automated erosion monitoring, and some preliminary evaluation tests were conducted on a shear-wave EMAT.

Many experiments have been conducted to establish the mechanism(s) of sulfidation and breakaway behavior of materials exposed to complex gas environments. Preliminary results are reported for chromium and Incoloy 800 specimens that were preoxidized in low-oxygen atmospheres and subsequently sulfidized in oxygen-free atmospheres.

Two of four experimental thermowells that were exposed for six runs in the U-Gas Pilot Plant were found to have suffered significant degradation, and these two components have been examined. In addition, the failure analysis of a sample of product gas piping from the BiGas Pilot Plant has been completed.

INTRODUCTION

Economical, reliable, and safe conversion of coal into clean and usable alternate fuels will be advanced through the use of durable materials of construction. The technical information base applicable to the behavior of materials in the operating environments characteristic of various coal-conversion processes is extremely limited. Hence, reliable materials selection and lifetime prediction are difficult to achieve. This program is designed to provide part of the materials information necessary for successful operation of coal-conversion systems. The present report is the twenty-third progress report submitted by ANL to the Office of Advanced Research and Technology, Office of Fossil Energy under Project Number 7106, "Materials Technology for Coal-conversion Processes".

The project includes four tasks: (A) Evaluation of refractories exposed to coal slag under conditions typical of those encountered in slagging gasification processes; (B) development and application of nondestructive evaluation methods; (C) evaluation of the corrosion behavior of commercial alloys; and (D) analyses of failed coal-conversion plant components.

Task A - Evaluation of Ceramic Refractories for Slagging Gasifiers

(C.R. Kennedy, R.J. Fousek, and S.W. Kreis)

Cores taken from the slag-refractory interface of six selected specimens exposed to a high-iron oxide acidic coal slag (base-to-acid ratio 0.5, $CaO/SiO_2 = 0.2$) in test run 12[1] have been polished and examined using reflected-light microscopy, x-ray analysis, and scanning electron microscopy with energy dispersive x-ray analysis (SEM-EDX). Electron microprobe analysis of these refractories is in progress and will be presented in the next report.

All of the alumina-chromia refractories were found to have reacted with iron oxide from the slag to form intermediate spinel layers. The thickness, coherence, and composition of these spinel reaction products varied according to the composition and density of the base refractory as detailed below.

As shown in Fig. 1, the fused-cast alumina refractory (Number 2) reacted with the slag to form a reasonably coherent 80 to 200-μm-thick layer of spinel. SEM-EDX (Fig. 2) indicates that the spinel is primarily composed of Fe and Al, with small amounts of Mg and Cr (indicating some cross-contamination from the chromia refractories). Intergranular attack was minimal. Also evident is the precipitation of crystallites within the slag (probably on cooling), which are also hercynitic-type spinels, $(Fe,Mg)Al_2O_4$. These observations are not unexpected; if the composition of the slag is represented on a ternary phase diagram[2] in terms of its three major constituents, i.e., SiO_2, Al_2O_3, and FeO (see Table I in Ref. 1), the primary phase predicted to crystallize from the slag is a hercynitic spinel solid solution.

The sintered 90 wt% Al_2O_3-10 wt% Cr_2O_3 refractory (Number 16, Fig. 3) and the chemically bonded 67 wt% Al_2O_3-32 wt% Cr_2O_3 refractory (Number 109, Fig. 4) also reacted with the slag to form reasonably coherent spinel layers. The thickness of the spinel layer was ∿100 μm for Number 16, whereas the layer on Number 109 varied from ∿200 to 400 μm. SEM-EDX (not shown) indicated that the spinels contained increasing amounts of Cr, in addition to Fe and Al and some Mg. Since wet chemical analysis indicated that ∿90% of the iron was in the +2 oxygen state, the general formula of the spinels may be represented by $(Fe,Mg)(Cr,Al)_2O_4$. Also evident was significant intergranular attack, especially in the chemically bonded refractory (Number 109), as seen in Figs. 5 and 6.

No evidence of intergranular attack was observed in the fused-cast 60 wt% alumina-27 wt% chromia refractory (Number 38, Fig. 7). The refractory initially consisted of a $(Fe,Mg)(Cr,Al)_2O_4$ spinel within an $(Al,Cr)_2O_3$ matrix. As can be seen in Fig. 8a, the $(Al,Cr)_2O_3$ matrix has reacted with iron oxide from the slag to form a spinel layer 50-100 μm thick that is closely related in composition to the as-received spinel inclusions.

Reflected-light images at low magnifications (Fig. 9a) revealed very little interaction of the slag with the fused-cast chrome-spinel refractory (Number 22). Indeed, this refractory demonstrated the least amount of corrosion in test run 12. At higher magnifications (Fig. 9b), a very thin (∿5-μm) layer of reaction product was visible adjacent to the original spinel matrix. SEM-EDX (Fig. 10) reveals that this layer is highly enriched with Fe and Al and depleted in Cr and Mg when compared with the spinel in the as-received material (Fig. 11). It also appears that the original spinel in the refractory has been enriched with Fe and depleted Mg to a depth of ∿1000 μm (not shown here). Thus, under these specific conditions, the indication is that Fe and Mg diffuse much faster in this complex Cr-rich spinel than does Al.

In contrast, examination of the chemically bonded 85 wt% alumina-10 wt% chromia refractory (Number 86), which suffered the most corrosion in test run 12, revealed the formation of a loose network of spinel reaction product 200-300 μm thick (Fig. 12), accompanied by very extensive intergranular attack. SEM-EDX results (not shown) indicated that the spinel was of the $(Fe,Mg)Al_2O_4$ type.

Also evaluated in test run 12 were several direct-bonded magnesia-chrome refractories. The reflected-light image of the slag-refractory interface of refractory Number 400 (42 wt% MgO-27 wt% Cr_2O_3) is shown in Fig. 13. The magnesia matrix (the dark gray, spotted phase) has been preferentially dissolved, leaving behind the Cr-rich spinel inclusions, which can be seen floating in the slag.

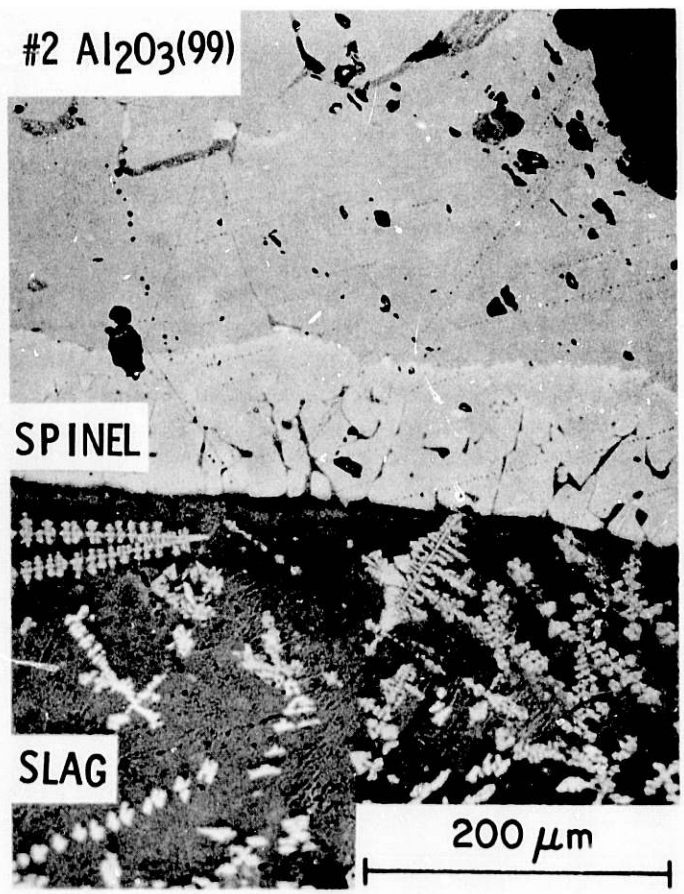

Fig. 1. Reflected-light Image of the Slag-Refractory Interface of the Fused-cast Alumina Refractory (Number 2) after Exposure to the High-iron Oxide Acidic Coal Slag.

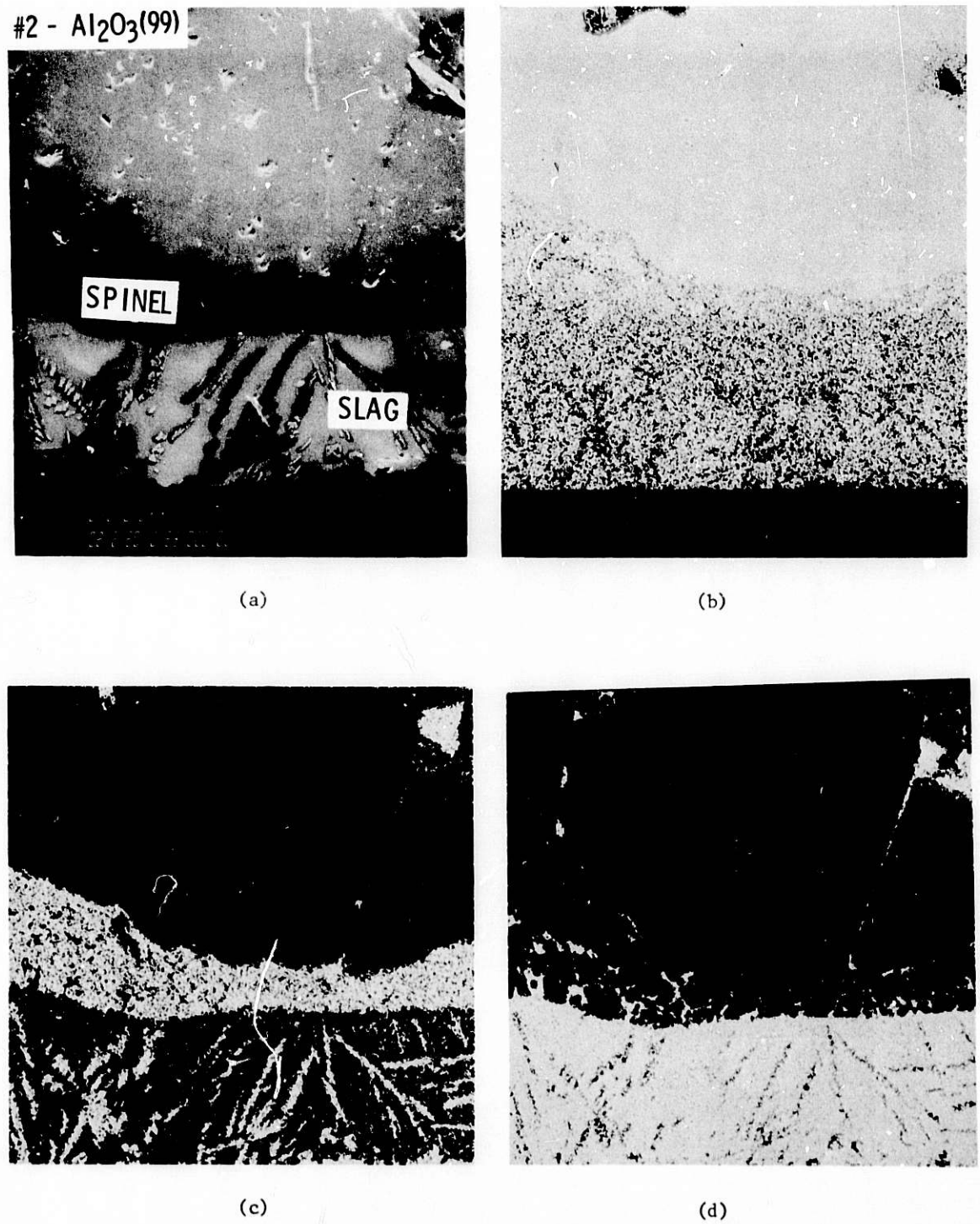

Fig. 2. SEM Photograph and Elemental Scans of the Slag-Refractory Interface of the Fused-cast Alumina Refractory (Number 2) after Exposure (Area Similar to That of Fig. 1). (a) SEM, (b) Al scan, (c) Fe scan, (d) Si scan.

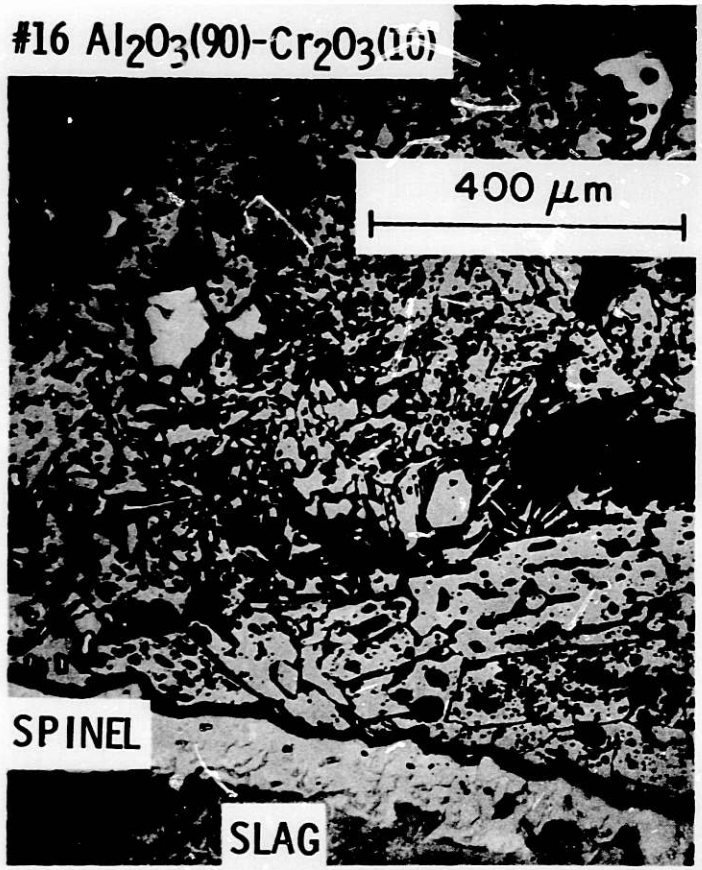

Fig. 3. Reflected-light Image of the Slag-Refractory Interface of the Sintered 90 wt% Alumina-10 wt% Chromia Refractory (Number 16) After Exposure.

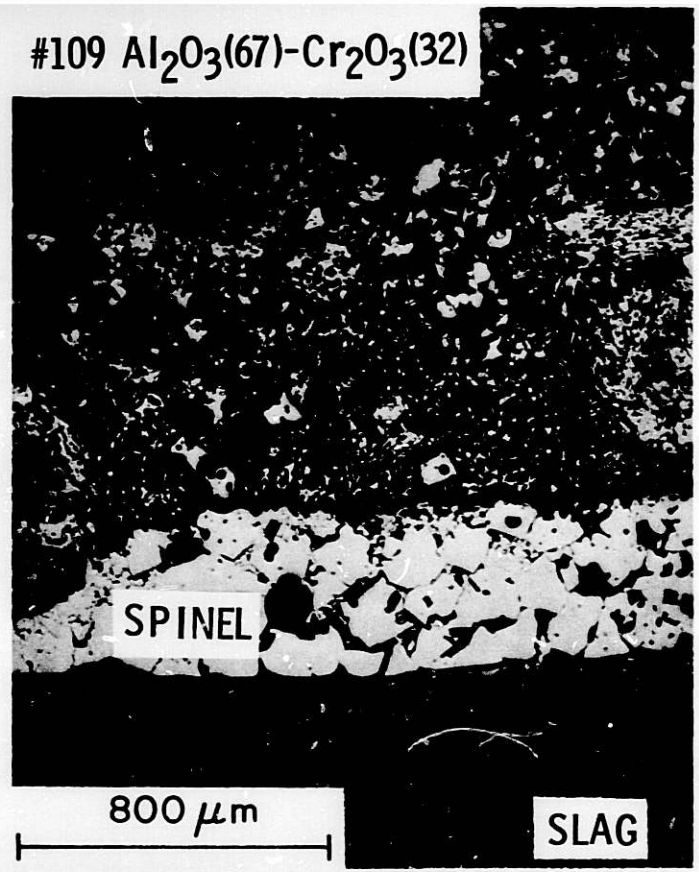

Fig. 4. Reflected-light Image of the Slag-Refractory Interface of the Chemically Bonded 67 wt% Al_2O_3-32 wt% Cr_2O_3 Refractory (Number 109) After Exposure.

Fig. 5. Reflected-light Image ∿1 mm from the Slag-Refractory Interface of Number 16, Showing Intergranular Attack.

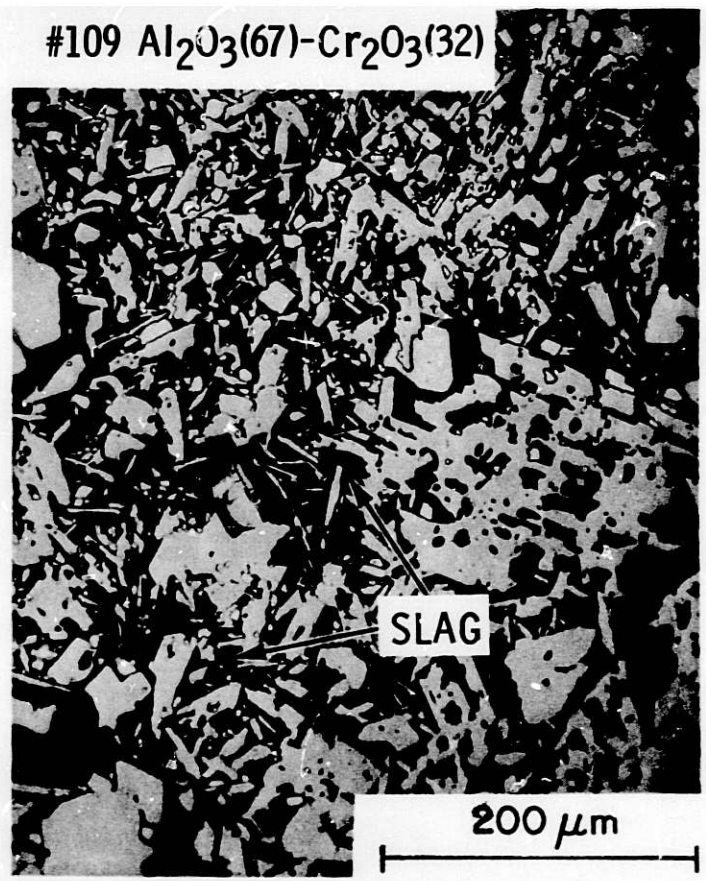

Fig. 6. Reflected-light Image ∿1 mm from the Slag-Refractory Interface of Number 109, Showing Extensive Nature of the Intergranular Attack.

Fig. 7. Reflected-light Image of the Slag-Refractory Interface of the Fused-cast 60 wt% Alumina-27 wt% Chromia Refractory (Number 38) After Exposure.

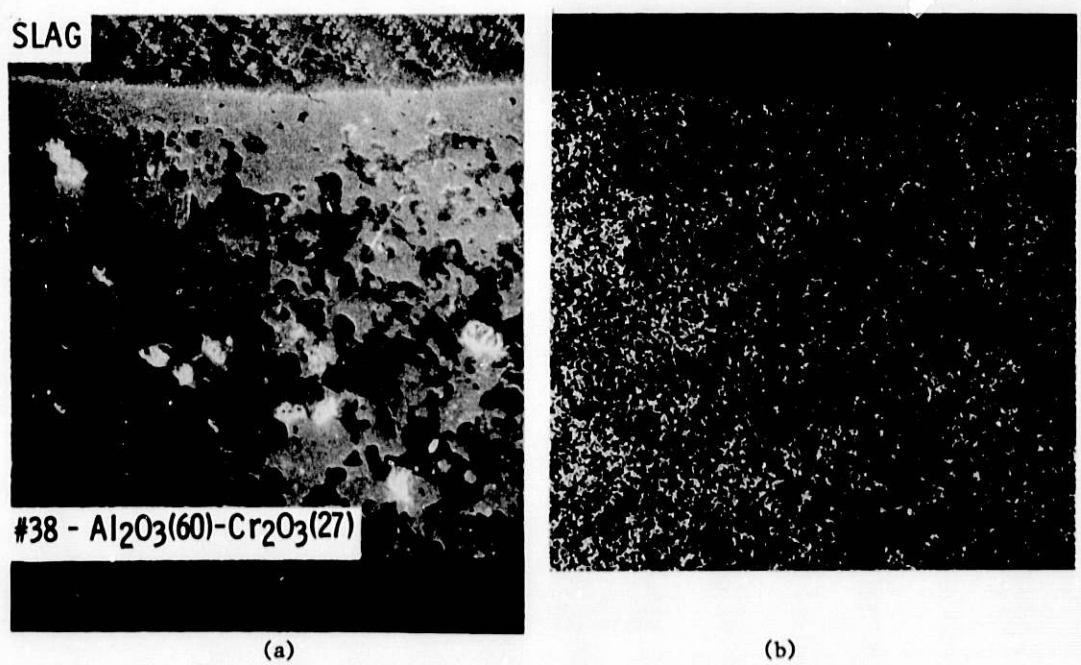

Fig. 8. SEM Photograph and Elemental Scans of the Slag-Refractory Interface of the Fused-Cast Alumina-Chromia Refractory (Number 38) After Exposure (Area Similar to That of Fig. 7). (a) SEM, (b) Cr Scan, (c) Al scan, (d) Fe scan, (e) Mg scan, (f) Si scan.

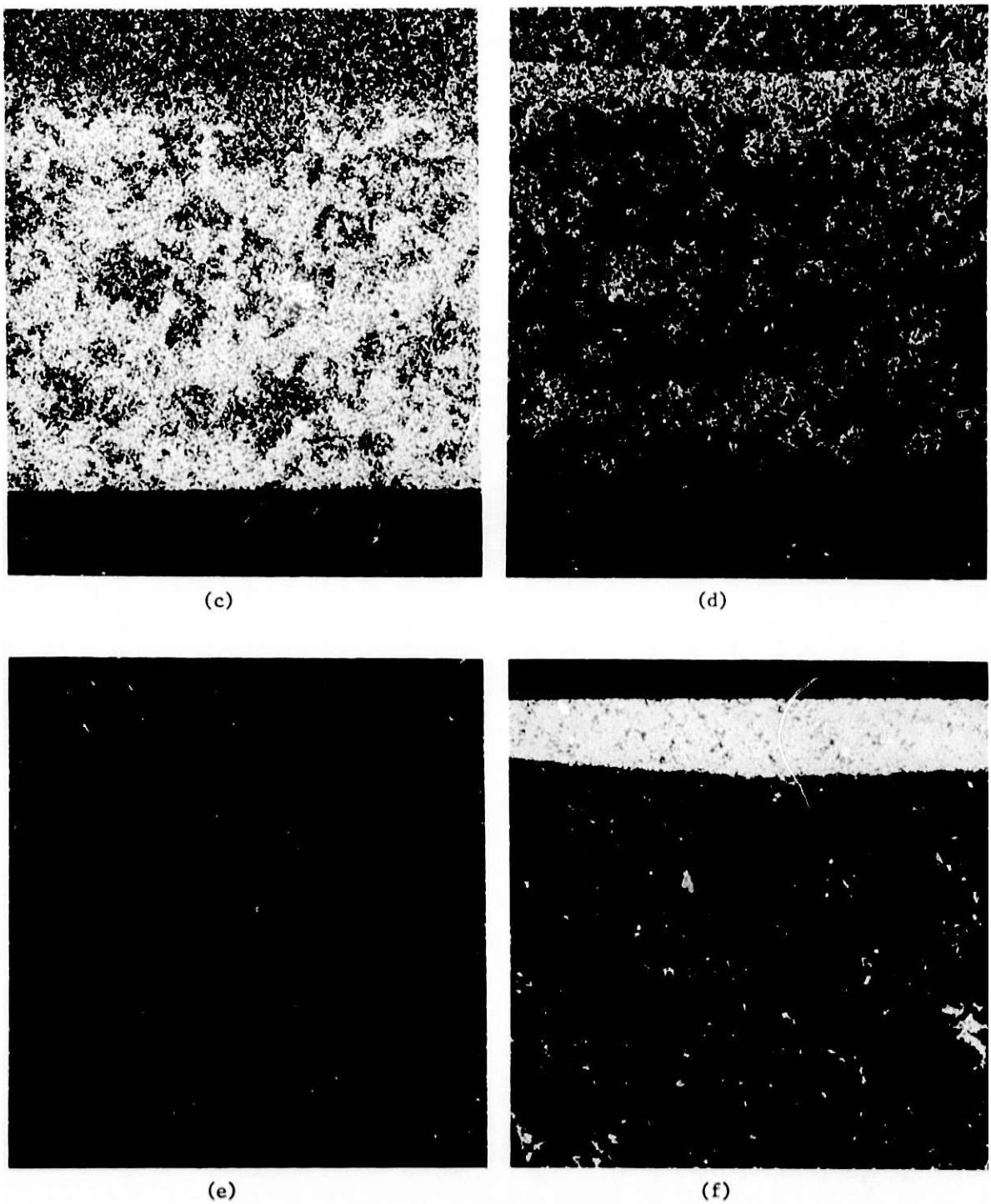

(c) (d)

(e) (f)

Fig. 8 (continued)

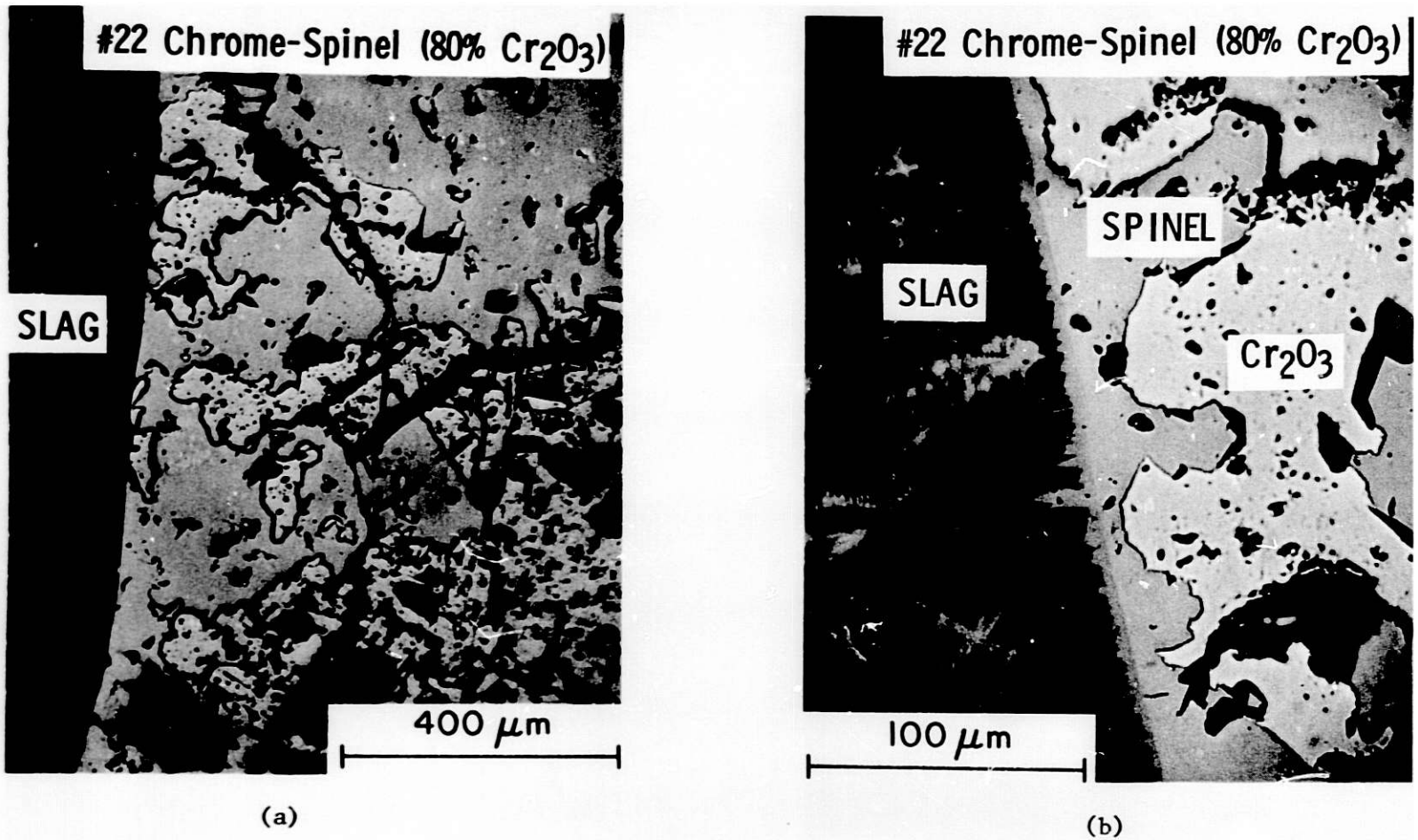

Fig. 9. Reflected-light Image of the Slag-Refractory Interface of the Fused-cast Chrome-spinel Refractory (Number 22) After Exposure. (a) Low magnification, (b) high magnification.

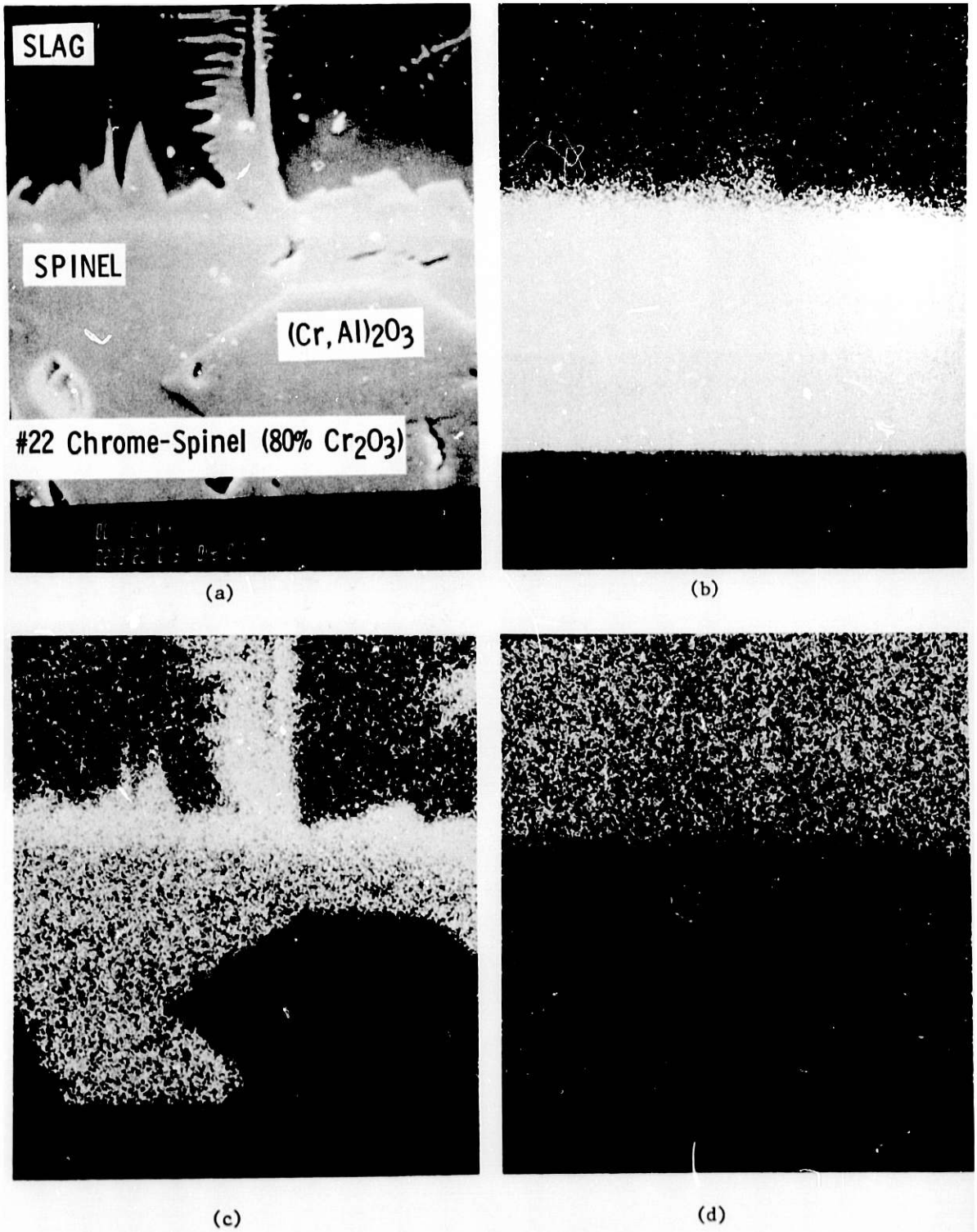

Fig. 10. SEM Photograph and Elemental Scans of the Slag-Refractory Interface of the Fused-cast Chrome-spinel Refractory After Exposure. (a) SEM, (b) Cr, (c) Fe, (d) Al, (e) Mg, and (f) Si.

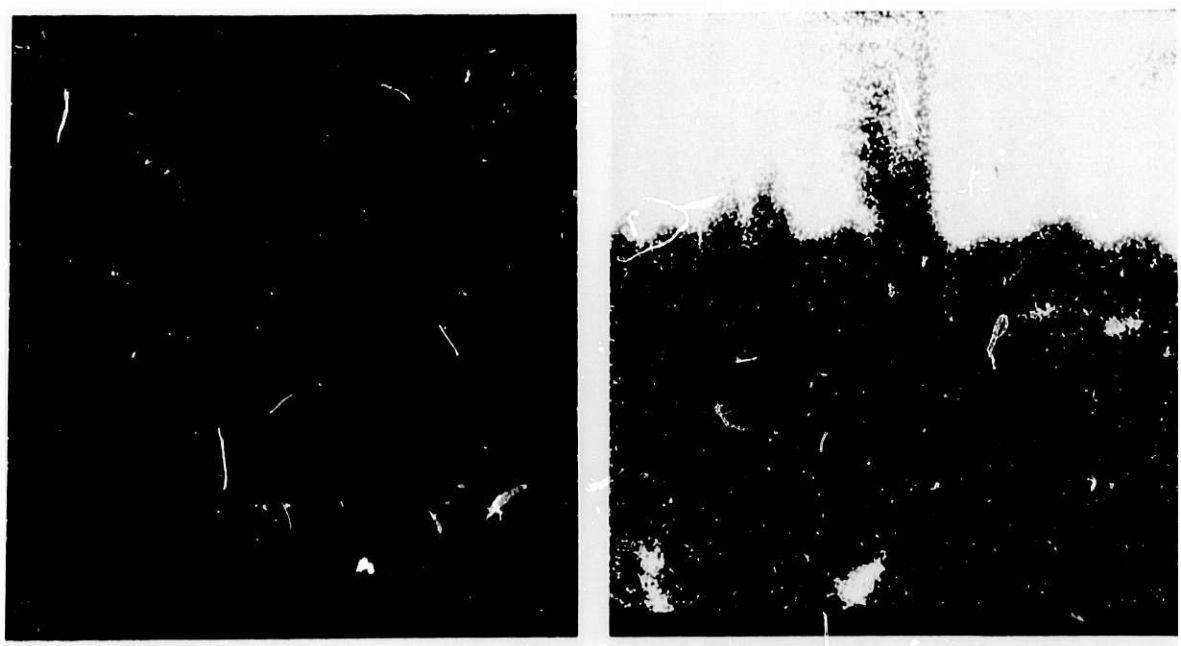

(e) (f)

Fig. 10 (continued)

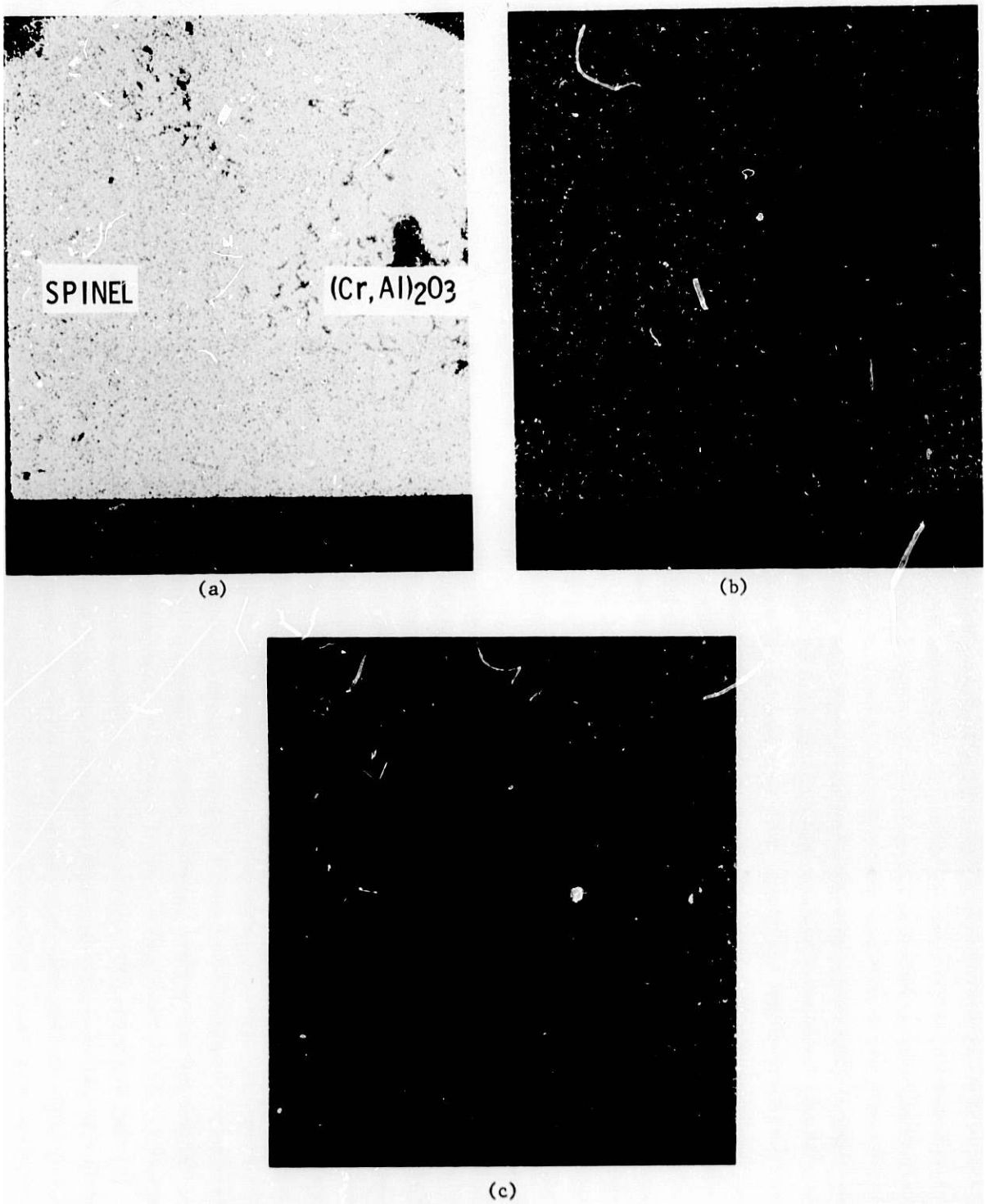

Fig. 11. Elemental Scans of the As-received Fused-cast Chrome-spinel Refractory. (a) Cr, (b) Fe, (c) Al, (d) Mg, and (e) Si.

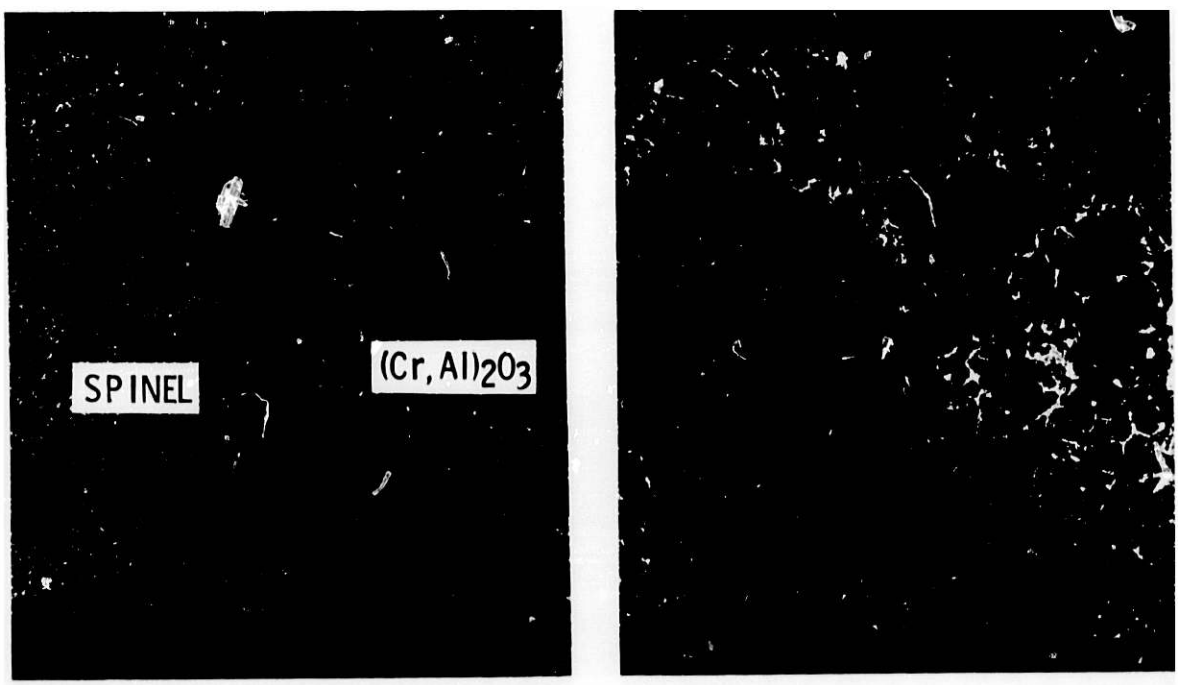

(d) (e)

Fig. 11 (continued)

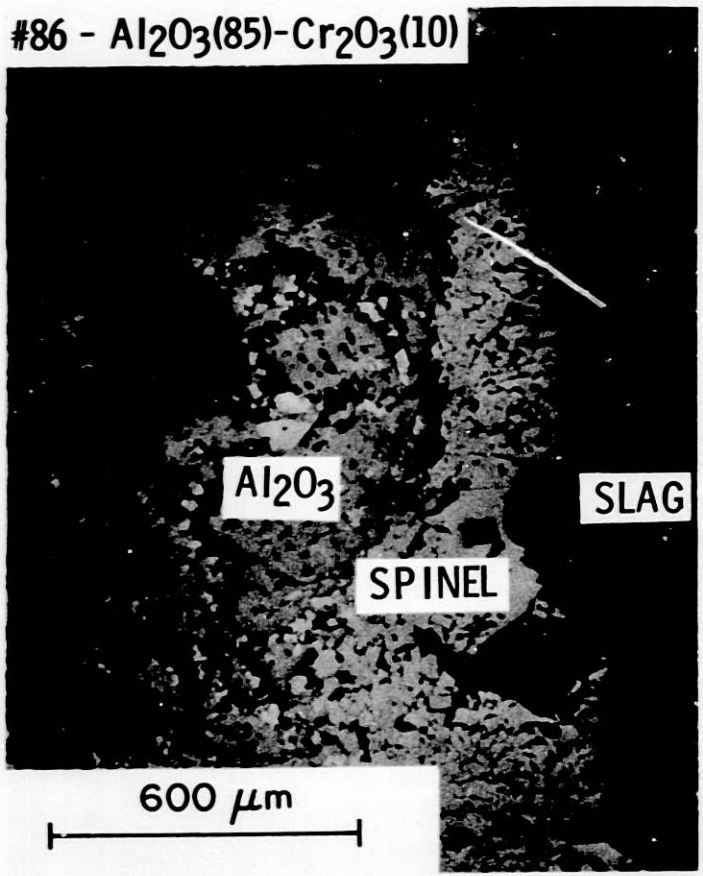

Fig. 12. Reflected-light Image of the Slag-Refractory Interface of the Chemically Bonded 85 wt% Al_2O_3-10 wt% Cr_2O_3 Refractory (Number 86) After Exposure.

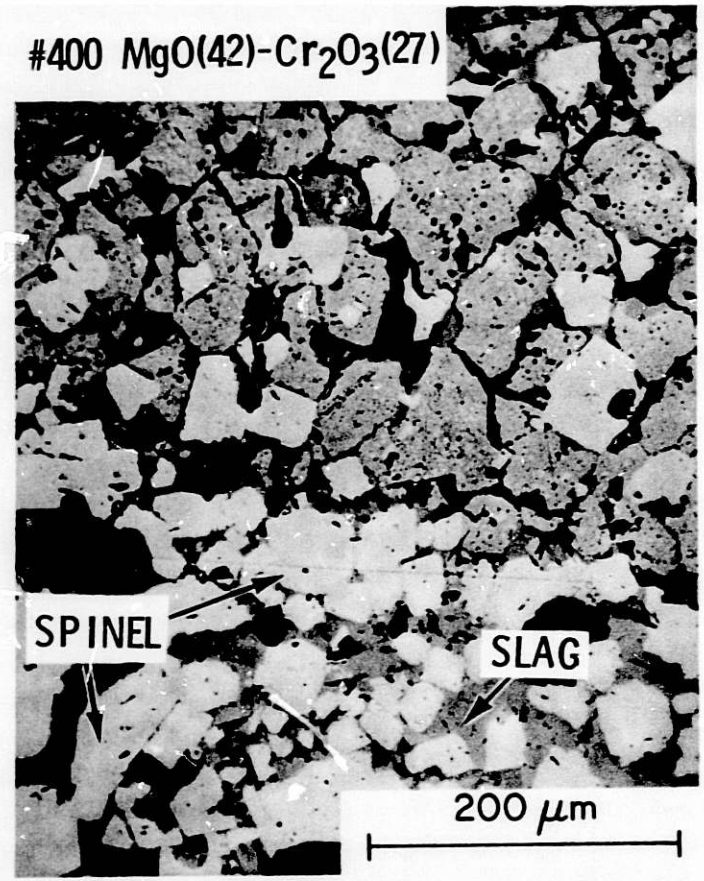

Fig. 13. Reflected-light Image of the Slag-Refractory Interface of the Direct-bonded Magnesia-Chrome Refractory (Number 400) After Exposure.

Task B - Development and Application of Nondestructive Evaluation Methods for Coal-conversion Processes *(W.A. Ellingson, C.A. Youngdahl, K.J. Reimann, and M.J. Caines)*

1. Erosive Wear: Detection and Monitoring

a. Metallic Transfer Lines

(1) Ultrasonic Studies - Pilot Plants

(a) Morgantown Energy Technology Center Fixed-bed Gasifier

A carbon steel tar-separation cyclone internally hardfaced with acoustically transparent B_4C and tested by METC on the fixed-bed coal gasifier was surveyed comprehensively by ultrasonic techniques during plant visits before and after operation. Less than 0.25 mm (<10 mils) of inlet-zone wall thinning was observed after nearly two weeks of plant operation, whereas previously >2.5 mm (> 100 mils) of thinning had been observed in a non-hardfaced carbon steel cyclone of the same design [inlet velocity 100 m/s (300 ft/s)] under comparable operating conditions and time. The ANL erosion scanner successfully followed the inlet-zone thinning of both of these cyclones during their respective periods of operation.

Ultrasonic examination of the hardfaced cyclone by direct wall contact techniques revealed that >2 mm (>80 mils) of thinning had occurred at some locations below the inlet zone and that an undulating internal surface had been produced during operation. Although METC reported that hardfacing of the entire internal surface had been ordered, ultrasonic evidence indicated that hardfacing was not applied below the inlet zone.

It was concluded that the B_4C hardfacing successfully reduced the rate of thinning by erosion-corrosion and should be more completely tested in a fully hardfaced cyclone designed to operate at a somewhat reduced inlet velocity.

In other work at METC, the inlet zone of a carbon steel tar-separation cyclone designed for operation at 65 m/s (200 ft/s) inlet velocity was surveyed. After a very brief period of operation on the gasifier, the cyclone exhibited up to 0.25 mm (10 mil) of thinning. Also, the solids separation cyclone was monitored, and little additional wear was found beyond that reported previously.[3]

(b) HYGAS Pilot Plant

The HYGAS high-pressure cyclone separator was again surveyed for additional erosive wear. Radiographs showed that the cyclone internal stainless steel cones had eroded through in some areas, and ultrasonic gauging provided values of least remaining thickness in the unsheathed portions of the stainless steel pressure wall. Locally, nearly half of the original 23-mm thickness has been lost by erosion. HYGAS reported that the unit will be used very conservatively until a replacement cyclone is available.

(c) Exxon Coal Liquefaction Pilot Plant (ECLP)

Installation of an automatic erosion scanner at ECLP was initiated in November during a plant turnaround period. Waveguides, clamping fixtures, and remote switching modules were put in place. Waveguides were similar to those shown in the previous report,[3] except that an ultrasonically reflective reference shoulder was machined near the tip of each guide. Copper foils 0.25 to 0.76 mm thick were used to acoustically couple waveguides to prepared surfaces on the piping. The sufficiency of pressure-coupling at the monitoring points at operating temperatures will be assessed after plant operations resume in January. Installation of conduits and cables by ECLP is near completion, and the scanner instruments have been completed and are undergoing tests at Argonne in preparation for installation in February.

(d) Solvent Refined Coal Liquefaction Pilot Plant

Additional field work described in the previous report[3] was carried out. Nine acoustic waveguides, each 127 mm long, were stud-welded to 1¼-in. (nominal) Schedule XXS Type 321 stainless steel piping, which replaces much of the 2-in. piping of the erosion-corrosion loop downstream of the dissolver. Three more such waveguides were attached to new 1½-in. piping at the preheater outlet. Four 610-mm-long, tapered, bimetallic waveguides[3] were stud-welded to a new 1½-in. (nominal pipe size) preheater coil and supported by struts clamped to the piping. Addditional instrument modules were installed to permit automatic accommodation of various waveguide lengths and the setting of an optional threshold level of the automatic gain control for each channel of the scanner. The new, tapered design of the long waveguides and the electronic modifications allow automatic scanning of all monitoring sites with measurement errors within ±0.05 mm after data reduction by the plant computer, to which the scanner is interfaced.

By early December, three weeks after slurry flow had resumed, the 1¼-in. piping, in which slurry flow velocity is highest, had lost 0.86 mm of thickness (maximum); computer plots of the thickness changes showed little scatter in the data. A broad wear peak was evident in each bend of 1¼-in. pipe, with lesser peaks in the 1½-in.-pipe bends. Detailed results of the current and previous monitoring will be given in a future report.

Development of 1.2-m-long waveguides is continuing in preparation for installation in the preheater during a shutdown period in late March. Addition of three more 0.6-m-long waveguides at that time is tentatively planned.

A collaborative paper on the long bimetallic waveguides has been accepted by ASNT for presentation at the spring meeting in March.

2. Electromagnetic Acoustic Transducer (EMAT)

Erosion monitoring by means of ultrasonic wall-thickness measurements has some shortcomings that could be eliminated by applying a different method to generate the ultrasonic energy. Application of piezoelectric transducers requires a good coupling between the transducer and the component to be measured, and some means of cooling if high-temperature use is contemplated. In the present monitoring system these two requirements are met by welding or pressure-coupling waveguides with cooling fins to the component, and cementing the transducer to the waveguide. This arrangement, however, reduces the flexibility of the system, since only one point of the component wall is monitored. An array of such waveguides is required to obtain an erosion profile.

A more versatile method that does not require a permanent transducer attachment (and thus allows profile scanning) would be advantageous for obtaining erosive wear profiles. The technique would, of course, have to be usable at elevated temperatures. Methods that might be considered include eddy currents (multiple-frequency or pulsed), radiographic tomography, and ultrasonics with a different sound-generation principle. The ultrasonic technique of electromagnetic acoustic sound generation appears to be the simplest, and at present the most highly developed, method to meet the aforementioned requirements.

a. Principles of EMAT Operation and Literature Review

Current literature was reviewed to assess the state of the art of EMAT technology. Work on EMATs up to 1976 was surveyed by R.E. Beissner in Ref. 4, which not only includes an elaborate bibliography but also describes the operating principles and the application of EMATs to particular inspection problems. Since 1976, efforts have been directed mainly toward improvement of EMAT performance, generation of particular wave types, and development of probes for specific inspection problems.[5-8] The development has progressed far enough that a commercial firm (WAZAU, Berlin, West Germany) is marketing small EMATs (receiving only) for angle beam transducer evaluation.

A large part of the literature reviewed in Ref. 4 describes the theory of generation of elastic (ultrasonic) waves in metals by an electromagnetic field. For a complete treatment of the theory, a simultaneous solution of the elastic force equations, the electron transport equations, and Maxwell's equations, subject to appropriate electromagnetic, acoustic and electronic boundary conditions, is required. However, for the application of interest, a theory based on the so-called "local approximation" is satisfactory. This approximation assumes that the electron velocity distribution at a point is dependent only on the field strength at that point, and only small changes in field strength occur over distances of a few electron mean free paths (classical skin depth). Material displacement is caused by the Lorenz force, which is generated by a static magnetic field and an induced high-frequency current density. The differential equation governing the material displacement can then be written in the form

$$\rho\ddot{\vec{u}} = \rho v \nabla^2 \vec{u} + \frac{1}{c} \vec{J}_e \times \vec{B}_o \quad , \tag{1}$$

where

ρ = material density,

$\vec{u}$ = material displacement vector,

∇^2 = La Placian differentiation operator,

v = acoustic velocity,

c = velocity of light,

$\vec{j}_e$ = electron current density vector,

and $\vec{B}_o$ = static magnetic field vector.

Substitution of an expression for the eddy current electron density yields

$$\vec{j}_e = (1-j)\,\frac{c}{\delta_c}\,\vec{n} \times \vec{H}\, e^{-x/\delta_c}\, e^{j(x/\delta_c - \omega t)} \quad , \tag{2}$$

where

$j = \sqrt{-1}$,

$\vec{n}$ = surface normal unit vector,

$\vec{H}$ = magnetic high-frequency field vector at the surface,

x = distance ,

and $\delta_c = \dfrac{c}{\sqrt{2\pi\omega\mu\sigma}}$ (the skin depth),

where ω = frequency,

μ = permeability,

and σ = conductivity.

Combining Eqs. (1) and (2) and solving for the displacement field at large x results in

$$u = \frac{j}{1+j\beta}\,\frac{\vec{B}_o \times \vec{n} \times \vec{H}}{4\pi\rho v\omega}\, e^{j(qx - \omega t)} \quad , \tag{3}$$

where $q = \dfrac{\omega}{v}$ (elastic wave number)

and $\beta^2 = \frac{1}{2}\, q^2\delta^2$ (dimensionless parameter) .

The peak displacement amplitude from Eq. (3) may be calculated as

$$u_{peak} = \frac{\vec{B}_o \times \vec{n} \times \vec{H}}{4\pi\rho v\omega\sqrt{1+\beta^2}} \, . \tag{4}$$

From the expression for peak displacement amplitude, the following points are evident:

(1) The direction of displacement depends on the vectorial product of the static magnetic field and the induced high-frequency field. By tailoring the magnet or coil design, longitudinal waves as well as two differently polarized shear waves can be generated.

(2) The displacement amplitude, and therefore the acoustic power, can be increased by either a stronger static magnetic field or a stronger high-frequency field; the latter can be accomplished by optimization of the coil design.

(3) For frequencies up to 25 MHz, the parameter β is smaller than unity and the displacement in various metals under the same driving condition is inversely proportional to the acoustic impedance of the metal.

These basic findings have been confirmed by experimental results reported in the literature.[9-11] Experimental EMATs were constructed using permanent and electromagnets for the static fields, with fields up to 8 T (80 kG) and, in the case of electromagnets, power consumption in the kW range. Peak pulse input powers of up to 30 kW were applied. The number of turns in the coils depended on the desired frequency of the acoustic wave. With coil tuning, frequencies of up to 70 MHz were achieved. The high-frequency coil design varied from flat spiral coils to multiple, specially shaped, or meandering coils, depending on the yoke configuration and the choice of acoustic waves to be generated. Directivity patterns of EMATs strongly depend on the coil configuration, since the coil geometry influences the tangential component of the high-frequency magnetic field. With meandering coils, the directivity can be changed by changing the frequency. With such a coil configuration, which is comparable to a phased array, surface (Rayleigh) and Lamb waves can be generated. Through use of a copper foil with an orifice to screen the active EMAT area, the beam width can be tailored to a desired size. The efficiency of EMATs is lower than that of piezoelectric transducers, and more signal amplification is generally required. However, better magnets and higher available input powers are constantly narrowing that margin. High static electromagnetic fields require cooling of the EMAT or pulsed power application.

Prototypical EMATs were experimentally tested for fatigue crack detection (Rayleigh or Lamb waves), flaw detection in gas pipelines, measurement of shear-wave attenuation in aluminum bars and rods, inspection of railroad rails, and thickness measurements. Specially designed EMATs were tested at high temperature (up to 1300°C) with excellent results. The signal amplitude in steel and aluminum increased with increasing temperature. More recently, prototype EMAT systems for inspection of Inconel steam generator tubes, for the examination of projectiles and welds, and for flaw detection were developed and tested. Similar work is being done to develop EMATs for inspection of stainless steel welds and for examination of nonconducting material components such as high-temperature ceramic tubes. Efforts to improve the performance of EMATs and adapt them to specific inspection problems are continuing here and abroad.

(b) Preliminary Experimental Results with a Prototype EMAT

A prototype EMAT was designed and constructed for ANL in cooperation with one of the earlier investigators, Bruce Maxfield. This transducer, shown in Fig. 14 with the associated preamplifier and matching network, employs an electromagnet for generation of the static field. The electromagnet has provision for cooling. A single high-frequency coil serves as generating and receiving coil. The single-coil feature requires a protective circuit in the preamplifier input to prevent overloading and burnout. The preamplifier, which is tuned with the coil to resonate around 10 MHz, has a gain of approximately 25 dB, with a band width of 2.5 MHz. The overload recovery time of the preamplifier is of the order of a few microseconds, so that wall thicknesses of 0.25 in. (6.3 mm) in stainless steel can be measured. The coil design is such that the EMAT propagates a shear wave in the direction of the center member of the E-shaped yoke.

The prototype EMAT was first tested on an aluminum plate 0.5 in. (12.5 mm) thick, with the test arrangement shown schematically in Fig. 15. A static magnetic field of 0.6 T (6 kG) was generated at the pole piece of the high-frequency coil when a power of 400 W was applied. The power was dissipated when a current of 18 A was passed through the coil. This power was sustained for only short periods of time to prevent overheating. The high-frequency coil was energized by an Arenberg Model 650 pulsed oscillator, tuned to the resonant frequency of the coil-preamplifier chain, with a peak-to-peak voltage of 400 V. The waveform of the input pulse, attenuated by 40 dB, is shown in Fig. 16.

The reflected echo amplitude from the bottom surface of the aluminum test block was rather small after it passed through the preamplifier, and an additional amplifier (Sonic Mark III receiver) was needed. The multiple reflections from the bottom surface of the aluminum test block are shown in the oscillogram of Fig. 17. The pulse separation is $\sim$8 μs, which, with a shear-wave velocity of 1.2×10^5 in/s (3.1×10^5 cm/s), indicates a path length of 1 in. (25 mm) or twice the thickness of the material. Figure 18 shows the first reflection on an expanded time scale. A comparison of Figs. 18 and 16 shows that very little pulse distortion occcurred in the material.

The voltage generated in the receiving coil was of the order of 1 mV (peak-to-peak). The efficiency of the system in the pulse-echo mode is therefore roughly 0.001/400, or -112 dB.

The tests were repeated with a Type 304 stainless steel test block of identical thickness under the same test conditions. The echo amplitude from the bottom surface of this test block was completely buried in noise. A rough calculation of the effects of material property changes on the generation and reception efficiency, using handbook values for electrical conductance, shows that the displacement amplitude in stainless steel will be smaller than that in aluminum by a factor of 6. Since, by reciprocity, the same effect will take place during reception, the received amplitude of echoes in aluminum will be 36 times larger than in stainless steel. The difference amounts to approximately 30 dB, not counting material attenuation. This explains the difficulty in detecting backwall echoes in the stainless steel test block.

Future work will concentrate on improving the system gain with a narrow-band amplifier, automating the switching of the static magnetic field, and evaluating the detection sensitivity for various metals encountered in fossil energy plant components.

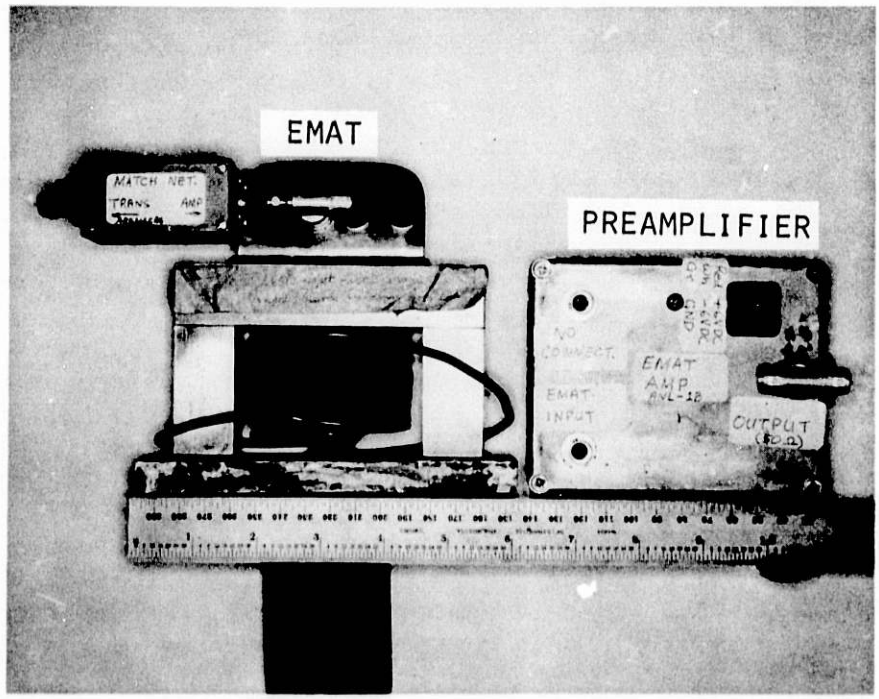

Fig. 14. Prototype EMAT with Electronics.

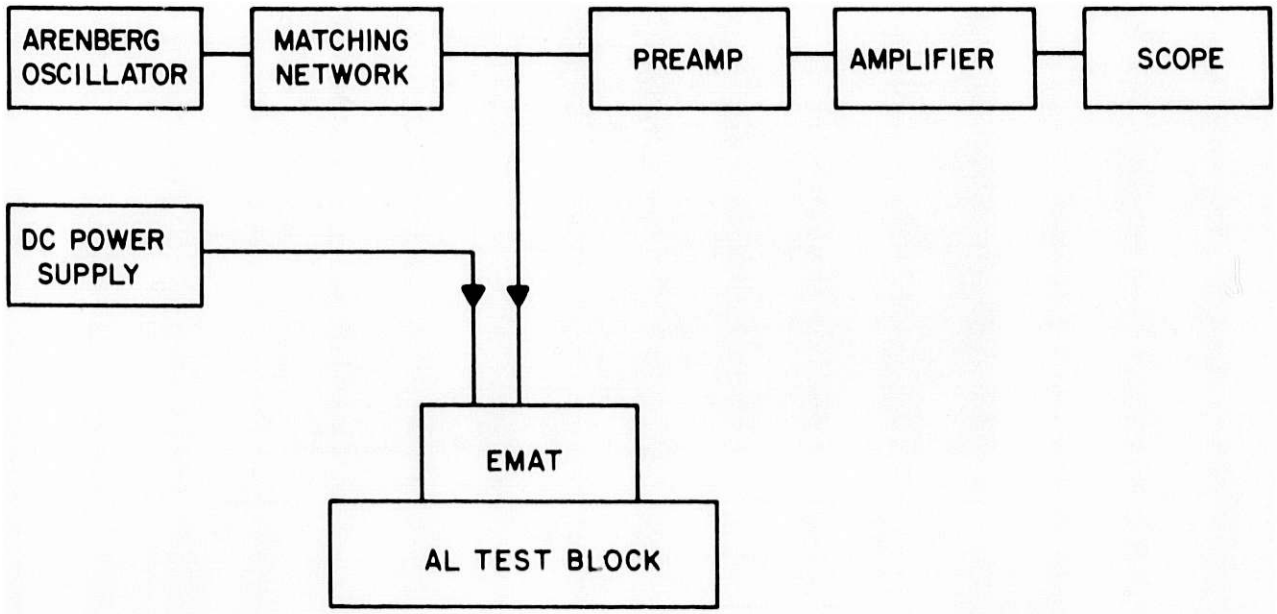

Fig. 15. Block Diagram of EMAT Test Setup.

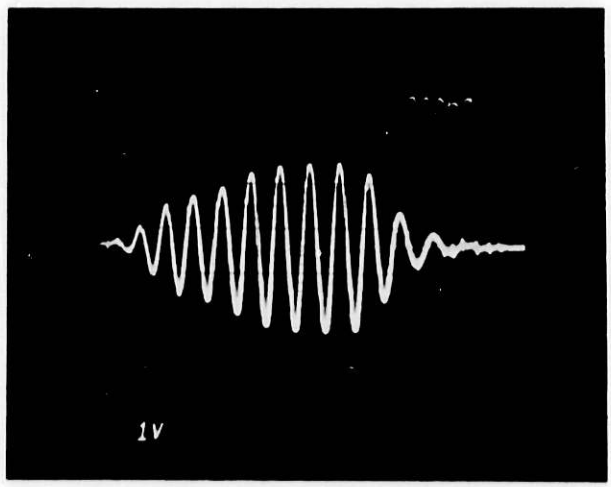

Fig. 16. High-frequency Input Pulse Waveform.

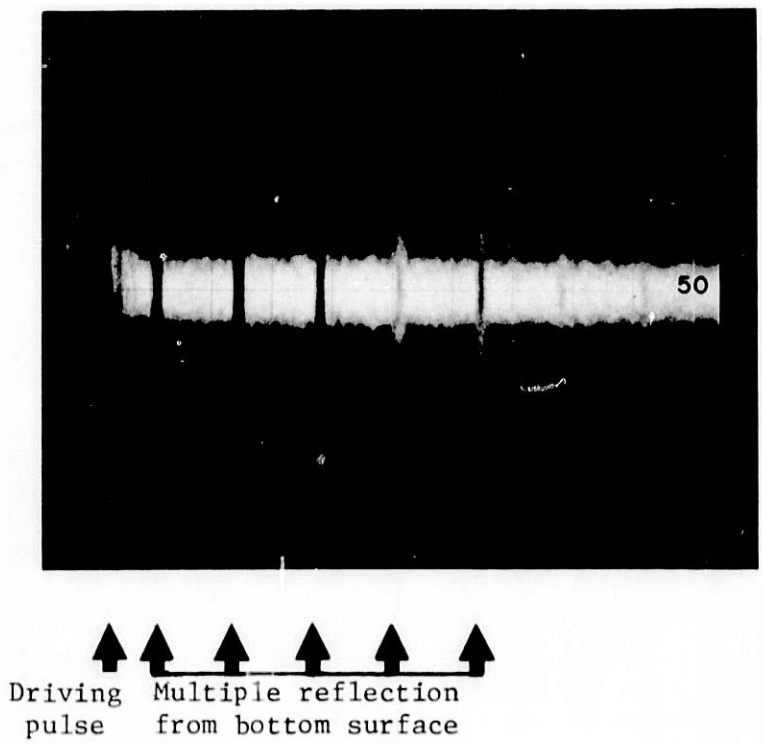

Fig. 17. Multiple Ultrasonic Reflections from Bottom Surface of Al Test Block as Received by EMAT.

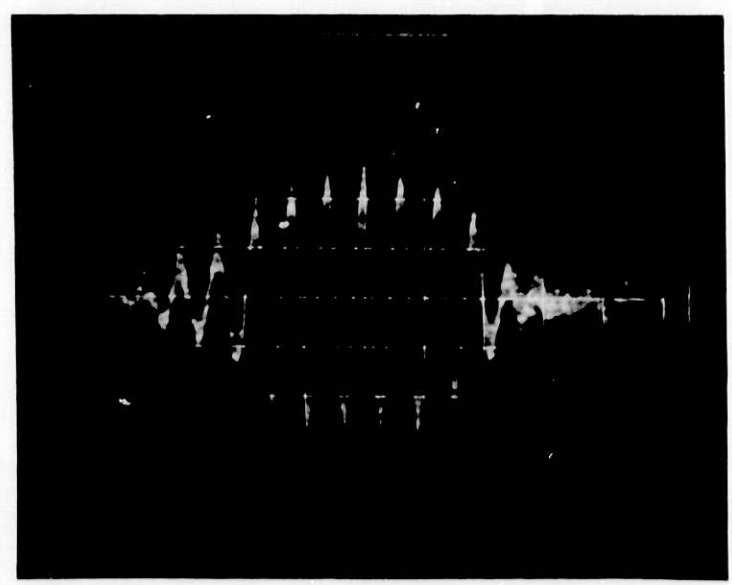

Fig. 18. Expanded First Return Echo Pulse from the Bottom Surface of the Al Test Block.

3. Refractory Installation Practices

a. Detection of Thermally Induced Acoustic Emissions from Refractory Concrete Materials

Work continues on preparation of the topical report.

4. Component Inspection

The preliminary slurry-loop design presented previously[1] was extensively modified because of difficulties with mechanical components and budget limitations. Completion of the new facility and initial test runs are planned for the next quarter.

Task C - Corrosion Behavior of Materials in Coal-conversion Processes
(K. Natesan)

The objectives of this program are to (1) experimentally evaluate the high-temperature corrosion behavior of iron- and nickel-base alloys in gas environments with a wide range of oxygen, sulfur, and carbon potentials, (2) evaluate deposit-induced hot corrosion behavior of heat exchanger and gas turbine materials with and without coatings after exposure to multicomponent gas environments, (3) develop uniaxial tensile data on four selected commercial alloys exposed to multicomponent gas enviroments, and (4) develop an approach that is based upon available thermodynamic and kinetic information for evaluating possible corrosion problems in various coal-conversion systems.

A state-of-the-art review[12] of the corrosion behavior of materials in coal gasifier environments has clearly established that sulfidation is the major mode of material attack in these systems and that a viable alloy should develop protective oxide scales on the material surface during the service life of a component. Furthermore, the experimental results have shown that for a given sulfur partial pressure, there exists a threshold in oxygen partial pressure above which a continuous protective scale is developed on the alloys. This threshold oxygen partial pressure is $\sim 10^3$ times the oxygen partial pressure for Cr-oxide/Cr-sulfide equilibrium. Even under these conditions, the majority of alloys tested in a mixed-gas environment exhibit breakaway or accelerated corrosion at some stage of exposure, depending on the temperature and partial pressures of sulfur and oxygen in the environment. It is imperative that alloys selected for application in coal-conversion systems should not exhibit breakaway corrosion during the service life of a component. However, very little is known mechanistically as to the cause(s) of the accelerated corrosion.

To evaluate the mechanism(s) of sulfidation and breakaway behavior of materials exposed to complex gas environments, sulfidation experiments are being conducted on specimens that have been preoxidized in low-oxygen gas environments. Alloys such as Incoloy 800, Type 310 stainless steel, and Inconel 671, and pure metals such as iron and chromium were preoxidized for 165 h in CO-CO_2-CH_4 gas mixtures and subsequently exposed for $\sim$125 h to H_2-H_2S gas mixtures. The oxygen partial pressure for the preoxidiation treatment was 9.2×10^{-18} atm at 871°C. The sulfur partial pressures for subsequent

treatment ranged from 2.9×10^{-13} to 2.0×10^{-7} atm. Upon completion of the exposures, the specimens were examined using an electron microprobe with EDX to identify the scale morphologies and to establish quantitatively the composition of the phases at different locations.

Figures 19 to 21 show the scale and scale/substrate regions of chromium specimens that were preoxidized and subsequently exposed to sulfur atmospheres at p_{S_2} values of 6.2×10^{-10}, 9.7×10^{-12}, and 2.9×10^{-13} atm, respectively. Table I gives quantitative elemental analyses of the scale and scale/substrate regions of the specimens shown in Figs. 19 and 20. The results show that the alloys developed a predominantly Cr_2O_3 layer $\sim$10 μm in thickness. In the interior of the scale, an oxygen concentration gradient exists for a depth of $\sim$20 μm. No sulfur was detected either in the scale or in the interior of the specimen.

Figures 22 to 24 show the scale and scale/substrate regions of Incoloy 800 specimens that were preoxidized and subsequently exposed to sulfur potentials at p_{S_2} values of 6.2×10^{-10}, 9.7×10^{-12}, and 2.9×10^{-13} atm, respectively. Quantitative elemental analyses of the scale and scale/substrate regions of these specimens are given in Table II. The results show that the samples exposed in these experiments developed a predominantly oxide layer with virtually no sulfur penetration. However, in contrast to pure chromium specimens, the Incoloy 800 specimens exhibited significant enrichment of titanium (as much as 4.8 wt%) in the scale. Furthermore, the specimen exposed to the lowest sulfur pressure ($p_{S_2} = 2.9 \times 10^{-13}$ atm) showed a much higher oxygen concentration and lower chromium concentration than would be expected based on the composition $(Cr,Ti)_2O_3$. Additional experiments at higher sulfur partial pressures and at different oxygen partial pressures are in progress to establish the mechanism(s) of oxidation/sulfidation of these materials upon exposure to mixed-gas environments.

Table I. Elemental Analyses of Chromium Specimens That Were Preoxidized at 9.2×10^{-18} atm and Subsequently Sulfidized in Two Different Oxygen-free Atmospheres

Sample Region	Elemental Analysis (wt %) Cr	Fe	Ni	O	S	Remarks
Sulfidized at $p_{S_2} = 6.2 \times 10^{-10}$ atm (Fig. 19)						
1	65.5	0	0.05	34.4	0	Cr_2O_3 scale
2	66.3	0.01	0.01	33.7	0	Cr_2O_3 scale
3	89.3	0.11	0.02	10.50	0.07	
4	94.6	0.08	0.08	5.24	0.01	
5	96.3	0.05	0.06	3.60	0	
6	99.8	0.07	0.07	0	0.03	Matrix
Sulfidized at $p_{S_2} = 9.7 \times 10^{-12}$ atm (Fig. 20)						
1	65.4	0.05	0.03	34.5	0.02	Cr_2O_3 scale
2	64.1	0.04	0.02	35.8	0	Cr_2O_3 scale
3	84.1	0.02	0.04	15.8	0	
4	89.3	0.03	0	10.6	0.02	
5	74.3	0.02	0.04	25.5	0.19	Cr_2O_3 particle
6	99.9	0.05	0	0	0	Matrix

Table II. Elemental Analyses of Incoloy 800 Specimens That Were Preoxidized at 9.2×10^{-18} atm and Subsequently Sulfidized in Three Different Oxygen-free Atmospheres

Sample Region	Elemental Analysis (wt %) Cr	Fe	Ni	O	S	Ti	Al	Remarks
	Sulfidized at $p_{S_2} = 6.2 \times 10^{-10}$ atm (Fig. 22)							
1	56.8	0.93	0.07	39.3	0	2.22	0.11	(Cr,Ti) oxide
2	57.4	0.80	0.18	35.6	0	4.74	1.52	(Cr,Ti) oxide
3	60.1	0.7	0.72	38.8	0	NA*	NA	
4	16.5	49.8	32.3	1.38	0			
5	15.8	50.1	32.8	1.19	0.05			
6	18.7	48.8	31.1	1.28	0			
7	21.8	45.1	30.3	1.03	0.04	0.033	0.50	Matrix
	Sulfidized at $p_{S_2} = 9.7 \times 10^{-12}$ atm (Fig. 23)							
1	50.4	2.4	1.5	40.9	0	4.8	0.13	(Cr,Ti) oxide
2	35.7	16.5	10.1	32.6	0	4.6	0.60	(Cr,Ti) oxide
3	20.5	47.0	30.4	1.3	0	0.2	0.66	Matrix
	Sulfidized at $p_{S_2} = 2.9 \times 10^{-13}$ atm (Fig. 24)							
1	46.7	0.75	0.32	42.7	0	4.8	0.30	(Cr,Ti) oxide
2	57.5	0.90	0.49	38.5	0	2.5	0.12	(Cr,Ti) oxide
3	23.0	45.5	29.5	1.22	0.01	0.12	0.53	Matrix

*NA: not analyzed.

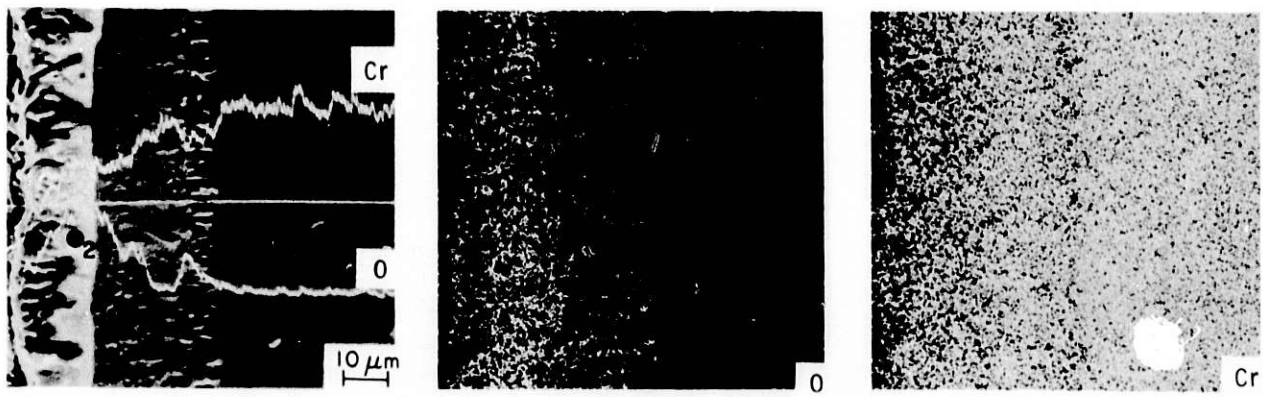

Fig. 19. SEM and EDX Photomicrographs of Chromium Specimen Preoxidized at p_{O_2} = 9.2 x 10^{-18} atm and Subsequently Sulfidized at p_{S_2} = 6.2 x 10^{-10} atm. The elemental analyses for regions 1 through 6 are given in Table I.

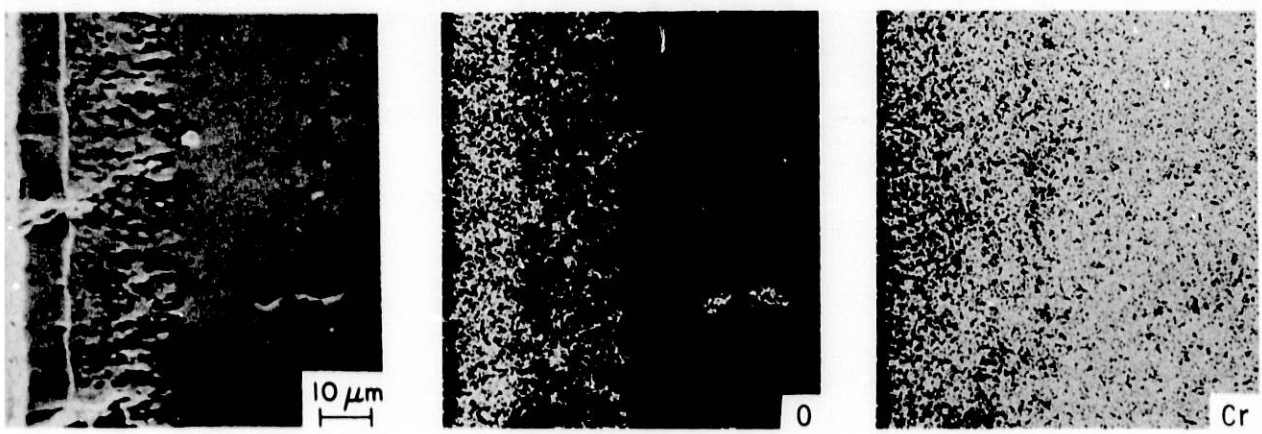

Fig. 20. SEM and EDX Photomicrographs of Chromium Specimen Preoxidized at p_{O_2} = 9.2 x 10^{-18} atm and Subsequently Sulfidized at p_{S_2} = 9.7 x 10^{-12} atm. The elemental analyses for regions 1 through 6 are given in Table I.

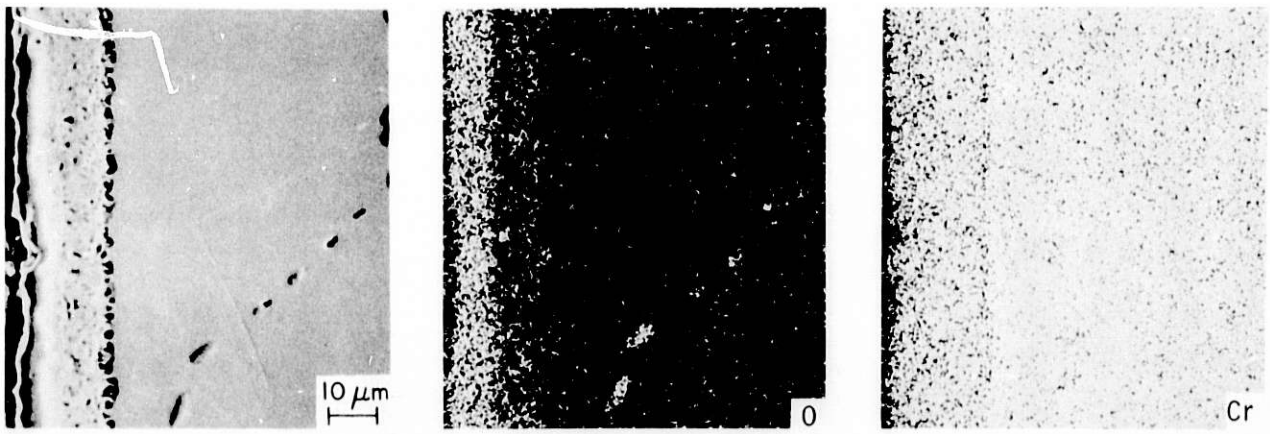

Fig. 21. SEM and EDX Photomicrographs of Chromium Specimen Preoxidized at p_{O_2} = 9.2 x 10^{-18} atm and Subsequently Sulfidized at p_{S_2} = 2.9 x 10^{-13} atm.

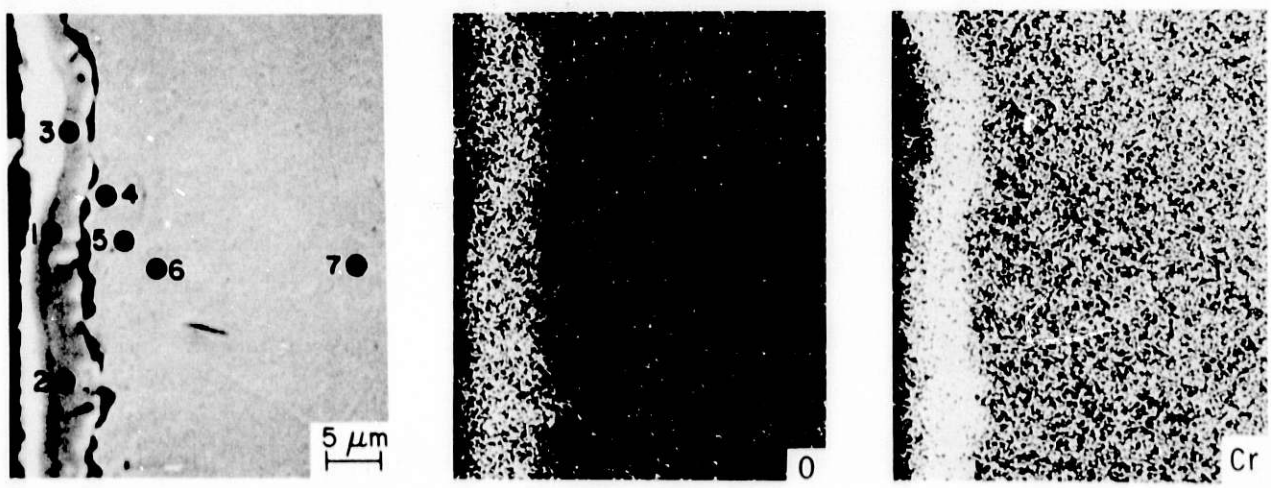

Fig. 22. SEM and EDX Photomicrographs of Incoloy 800 Specimen Preoxidized at p_{O_2} = 9.2 x 10^{-18} atm and Subsequently Sulfidized at p_{S_2} = 6.2 x 10^{-10} atm. The elemental analyses for regions 1 through 7 are given in Table II.

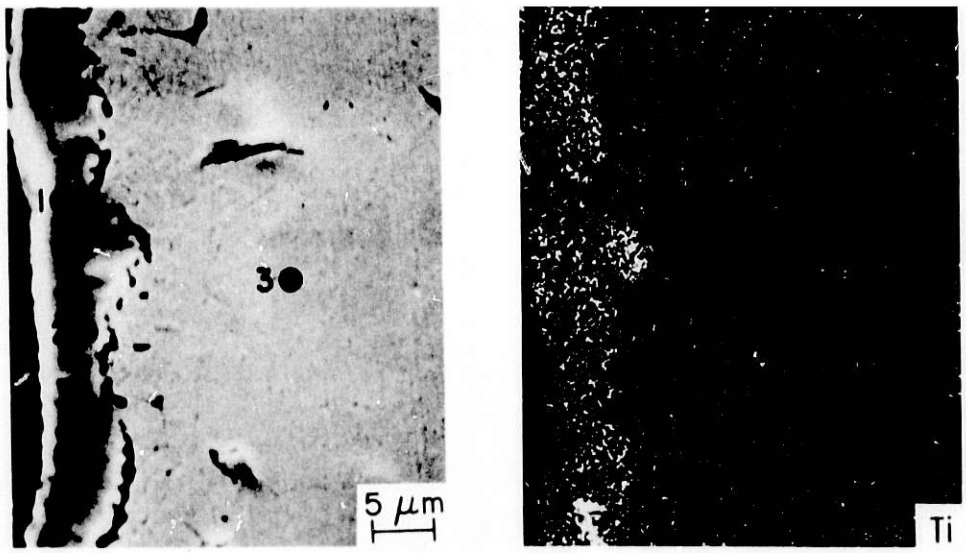

Fig. 23. SEM and EDX Photomicrographs of Incoloy 800 Specimen Preoxidized at p_{O_2} = 9.2 x 10^{-18} atm and Subsequently Sulfidized at p_{S_2} = 9.7 x 10^{-12} atm. The elemental analyses for regions 1 through 3 are given in Table II.

Fig. 24. SEM Photomicrograph of Incoloy 800 Specimen Preoxidized at p_{O_2} = 9.2 x 10^{-18} atm and Subsequently Sulfidized at p_{S_2} = 2.9 x 10^{-13} atm. The elemental analyses for regions 1 through 3 are given in Table II.

Task D - Failure Analysis *(D.R. Diercks, G.L. Fogle, and G.M. Dragel)*

1. Experimental Thermowells for IGT Ash Agglomerating (U-Gas) Gasifier

Seven experimental thermowells have been prepared for trial exposure in the IGT Ash Agglomerating Gasifier (U-Gas) Pilot Plant, as described in previous reports.[3,13] The alloys and coatings used to fabricate the lower portions of the experimental thermowells, which are subject to corrosive and erosive attack in service, are listed in Table III. For the first series of exposures, thermowells 2, 3, and 7 were installed at positions approximately 1.1, 1.4, and 2.3 m (3.5, 4.5, and 7.5 ft), respectively, above the normal operating height of the bed. Thermowell 1, which is an uncoated Haynes 188 thermowell identical to thermowell 2, was installed at a somewhat more erosive location approximately 0.4 m (1.4 ft) above the top of the bed. The thermowells did not contain thermocouples.

A total of six plant runs, each approximately four to five days long, were completed with the first four experimental thermowells in place. All of these runs were made using relatively high-sulfur Eastern coals, and the bed operating temperature was typically in the range from 1024 to 1066°C (1875 to 1950°F). Thermowells 1 and 3 were found to be leaking after the completion of the sixth run, and a decision was made to remove all four thermowells for post-exposure examinations. Some of the results obtained from these examinations will be discussed here.

The macroscopic appearance of thermowells 1, 2, 3, and 7 after removal from the U-Gas Pilot Plant is shown in Fig. 25. Only the last ∿6 to 8 cm of each thermowell projected into the gasifier beyond the inner surface of the refractory lining, and the damage was almost entirely confined to this region. Both thermowells 1 and 7 suffered significant loss of material at the tip, and in both cases this damaged region faced downward toward the fluidized bed during the exposure. The remaining portions of these two thermowells exhibited much less damage, with only slight surface roughening or local spallation of the coating noted. Thermowells 2 and 3 did not experience any severe attack at the tip, and the overall surface roughening was comparable to that seen in thermowells 1 and 7 away from the tip.

In view of the relatively minor attack experienced by thermowells 2 and 3, it was decided to set these two assemblies aside for further exposures, and to confine the present examinations to thermowells 1 and 7. These latter two thermowells were therefore sectioned both circumferentially and axially, with the axial sections intersecting the severely attacked regions at the tips. Portions of an axial metallographic section from thermowell 1, which was fabricated using uncoated Haynes 188, are shown in Fig. 26. The surface at the top of Fig. 26a is the heavily eroded outward-facing sidewall of the end plug; the weld-metal region joining the end plug to the tubular portion of the thermowell has been completely eroded away. The less severely attacked inner surface of the end plug, which was not exposed to the gasifier environment until perforation occurred, is shown to the left of this micrograph. This thermowell was uncoated, but a surface layer that differs from the interior of the sample in etching characteristics is clearly visible. This suggests that the erosive wear at the tip of thermowell 1 was accompanied by corrosive attack. The microstructure shown in Fig. 26b, from a different location at the outer surface of the end plug, indicates that several distinct phases are present in the surface layer.

The other failed thermowell that was examined here was thermowell 7, which was made of aluminized Type 310 stainless steel. Figure 27a shows the microstructure present at the outer surface of the tubular sidewall away from the region of heavy erosive wear at the tip. The Type 310 stainless steel base metal is visible near the bottom of the micrograph, and the multilayered aluminized coating is seen above it. Several cracks extend into the coating from the outer surface, and these cracks appear to be filled with a corrosion product, probably an oxide. However, the general adherence of the coating to the substrate is good, and the coating appears to be providing reasonable protection against erosive wear and corrosive attack at this location.

Figure 27b shows the microstructure at the outer surface of the end plug in the highly eroded region at the tip of thermowell 7. The aluminized coating has been entirely lost here, and the Type 310 stainless steel base metal is experiencing extensive intergranular and intragranular corrosive attack as well as erosive wear.

Because corrosive attack appears to have played an important role in the failures of thermowells 1 and 7, samples from these two thermowells were examined by SEM and electron microprobe in order to identify the corrosion product phases present. Selected microprobe results for thermowell 1 are shown in Figs. 28a through d. The region shown in the backscattered electron image of Fig. 28a is at the outer surface of the end plug, somewhat away from the region of most severe erosive attack. Both intergranular and intragranular precipitates are clearly visible. The accompanying x-ray images of Figs. 28b through d identify the grain-boundary phase as chromium oxide near the surface and a mixture of chromium oxide and sulfide farther in. The fine intragranular precipitates appear to be sulfides, probably again in combination with chromium. The distribution of iron, nickel, and cobalt (not shown here) showed no unusual features except that iron tended to be somewhat concentrated intragranularly near the surface, and all three elements were depleted in the grain-boundary regions near the surface.

Thermowell 7 was examined in regions where the aluminized coating was still intact as well as in areas of severe attack. A series of photographs from an intact region is shown in Fig. 29. The aluminized coating in the top two-thirds of the photographs is seen to consist of three layers, namely (1) an outer layer high in Al, Fe, and Cr and low in Ni, (2) a thin, intermediate layer high in Ni and Al and depleted in Cr and Fe, and (3) a thicker third layer somewhat higher in Al and Cr and lower in Ni than the underlying Type 310 stainless steel substrate. The outer layer of the aluminized coating contains numerous cracks which appear to stop at the interface with the second layer. These cracks are seen here to contain high aluminum concentrations, and a separate analysis (not shown here) on an instrument more sensitized to low atomic number elements also showed them to contain high oxygen levels. The phase in the cracks is thus identified as Al_2O_3. The sulfur scan of Fig. 29 indicates that no significant sulfidation occurred in this region.

In regions of heavy attack on thermowell 7, the aluminized coating was, of course, completely absent. X-ray images of this area showed considerable chromium oxide and sulfide formation in the Type 310 stainless steel substrate, both in the surface scale and as intergranular and intragranular phases. No nickel sulfide formation was indicated.

As stated above, thermowells 2 and 3 emerged from the first series of exposures in apparently good condition, and they have been set aside without destructive examination for further exposures at a later date. Thermowells 4, 5, and 6 have been installed in the U-Gas Pilot Plant but have not yet been exposed, since the plant is presently down for modifications. The present series of exposures is anticipated to begin again in mid-February with the resumption of operations at the pilot plant.

2. Product Gas Line from BiGas Plant

The previous report[3] described initial results from the analysis of a failed product gas line (Schedule 140, Type 304 stainless steel) from the BiGas Coal Gasification Pilot Plant. The failure consisted of a circumferential crack extending approximately 270° around the pipe in the vicinity of a weld to an adjoining tee. Water, presumably due to condensation, was found inside the failed pipe when it was disassembled; the water had a pH of 8.5 and a chloride content of 4.5 ppm. The cracking present in the failed pipe was found to be intergranular and highly branched, and the application of ASTM Procedure A262, Practice A to the sample revealed a moderate level of grain-boundary sensitization to be present.

Both fracture surfaces and the polished metallographic specimens from the failed pipe were then examined in the SEM. The appearance of the fracture surfaces in the SEM reflected the intergranular nature of the fracture, but no other unusual features were noted. In particular, x-ray analyses of the region did not indicate the presence of either chlorides or sulfur. However, the SEM examination of a polished metallographic section from near the inner surface of the pipe revealed extensive grain-boundary attack at and near the inner surface, and x-ray scans of these regions showed that the corrosion product contained sulfur, probably in the form of mixed chromium and iron sulfides. While these sulfides were commonly found at and near the inner surface, they were totally absent in both metallographic and fracture-surface specimens taken from the interior of the pipe. It thus appears that these sulfides formed prior to cracking as a result of prolonged elevated-temperature contact with the sulfur-containing product gas from the BiGas gasifier.

The presence of these sulfides at the inner surface of the failed piping immediately suggested the possibility that failure was due to polythionic acid-induced IGSCC. Failures of this sort are often observed in petrochemical plant components, where the polythionic acid ($H_2S_xO_6$, where x = 3 to 5) results from the reaction of condensate formed during shutdown with a previously existing sulfidic scale in the presence of oxygen. The necessary sulfidic scale, condensation, and oxygen were all present in the failed BiGas piping, and the failure exhibited the characteristic highly branched intergranular cracking in a sensitized austenitic microstructure that is generally associated with polythionic acid cracking. The tensile stress required to drive a polythionic acid cracking process could easily be supplied either by the residual stresses present in the vicinity of the weld or by differential thermal expansion effects at the austenitic-ferritic steel junction.

The other possible corrosive species that could lead to the sort of cracking seen here include chlorides, caustics, and dissolved oxygen. Although chloride-induced IGSCC is possible in a sufficiently sensitized microstructure, this mechanism seems unlikely here in view of the totally intergranular nature of the cracking, the very low level of chlorides (~4.5 ppm) found in condensate present in the failed pipe, and the absence of detectable chlorides on the fracture surface. Similarly, the relative lack of oxide formation in the cracks makes caustic- or oxygen-induced cracking seem less likely. Therefore, the present failure has been attributed to polythionic acid-induced IGSCC. Purging the product gas line with dry nitrogen or a similar inert atmosphere at each shutdown was recommended as a means of preventing polythionic acid formation due to the contact of condensate and oxygen with sulfidic scale at the inner surface of the gasifier piping.

Table III. Summary of Alloys and Coatings Used to Fabricate Lower Portions of Experimental Thermowells

Thermowell No.	Alloy	Coating
1	Haynes 188	none
2	Haynes 188	none
3	Incoloy 800	Cr-Al-Hf
4	Incoloy 800	aluminized
5	Type 310 stainless steel	Cr-Si
6	Type 310 stainless steel	Cr-Al-Hf
7	Type 310 stainless steel	aluminized

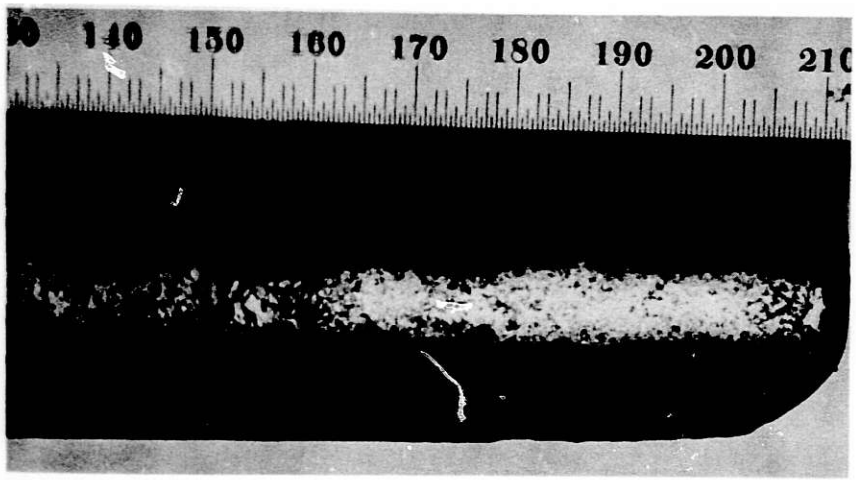

(a)

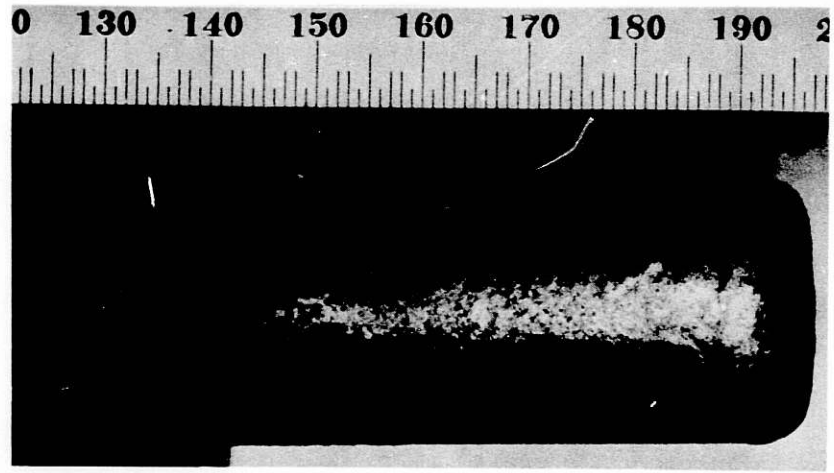

(b)

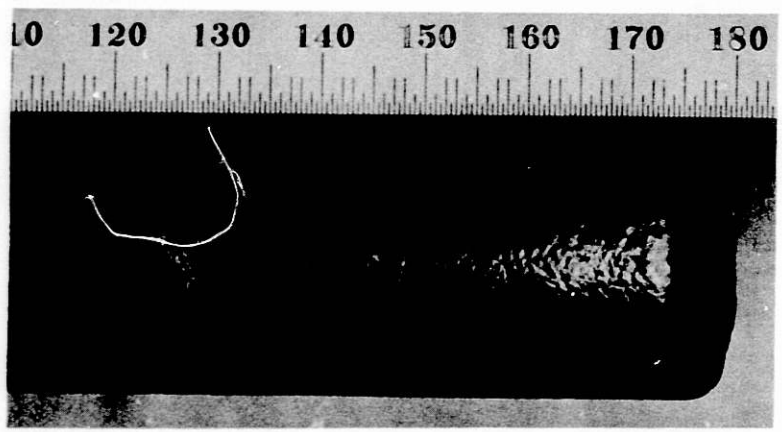

(c)

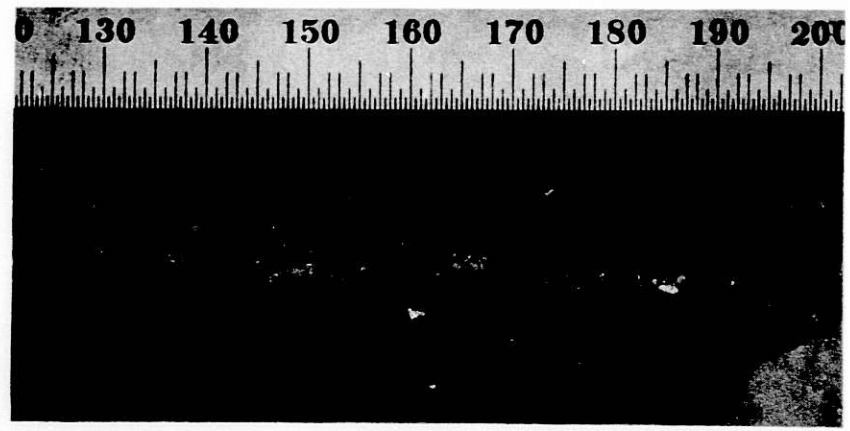

(c)

Fig. 25. Macroscopic Appearance of Four Experimental Thermowells after Exposure to Six Runs in U-Gas Pilot Plant Gasifier. (a) Thermowell 1, (b) thermowell 2, (c) thermowell 3, and (d) thermowell 7.

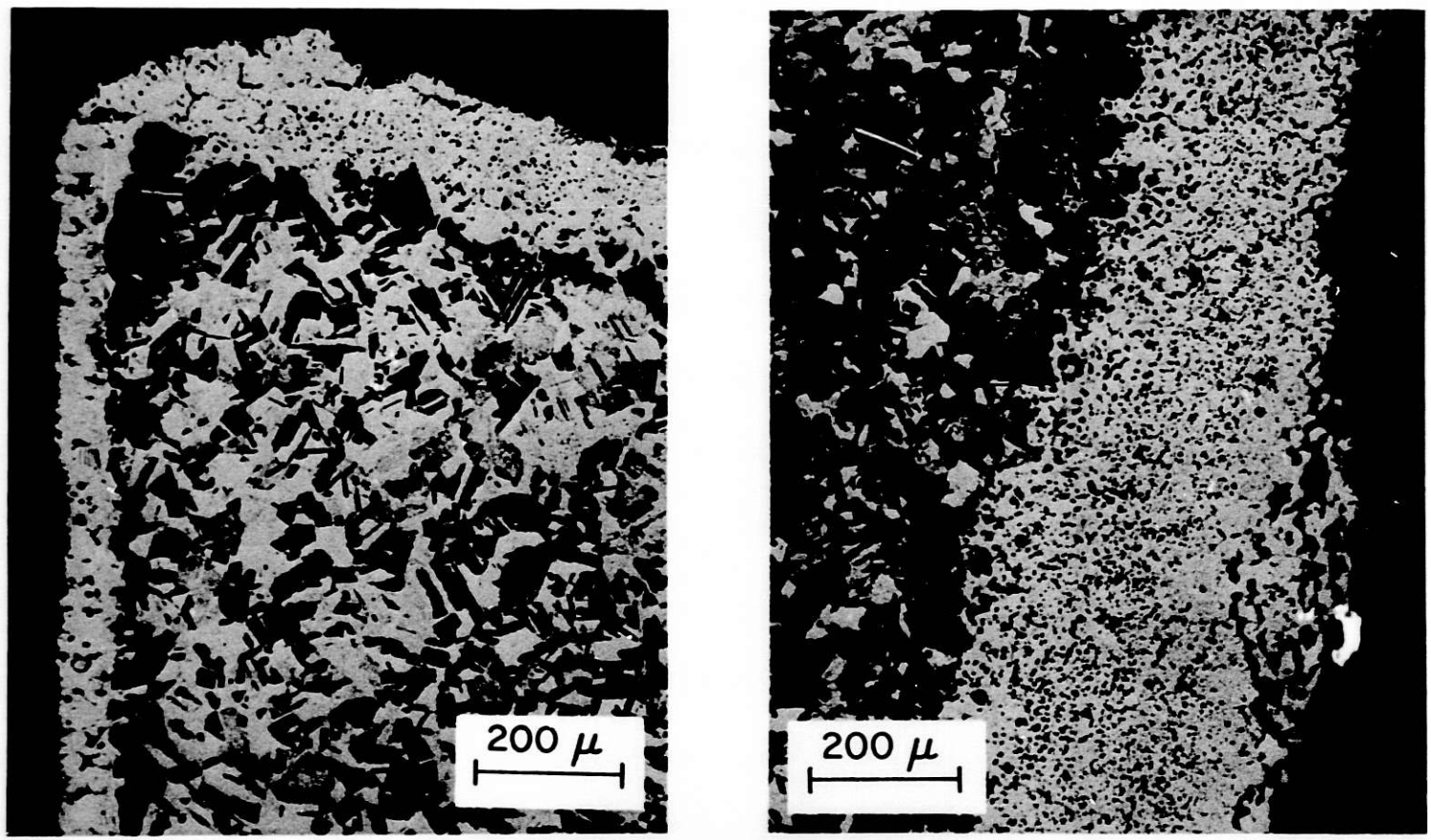

(a) (b)

Fig. 26. Microstructures at Two Locations in Axial Section Through Heavily Eroded Region in End Plug of Thermowell 1. (Etchant - 100 ml HCl, 15 ml HF, 30 ml H_2O_2).

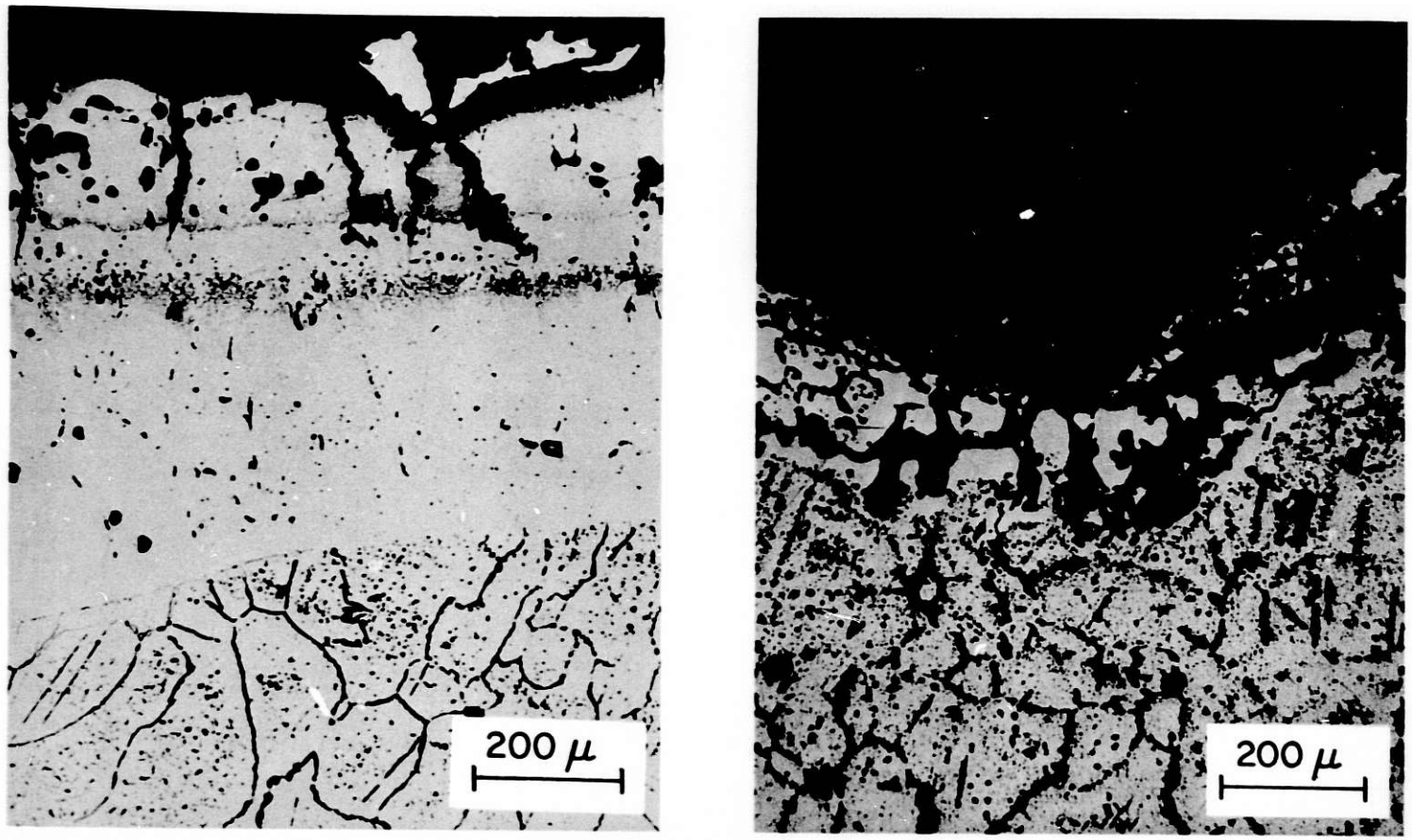

(a) (b)

Fig. 27. Microstructures at Two Locations in Axial Section Through Thermowell 7. (a) Intact location in sidewall, and (b) heavily attacked region in end plug. (Etchant - 10% oxalic acid in water electroetch).

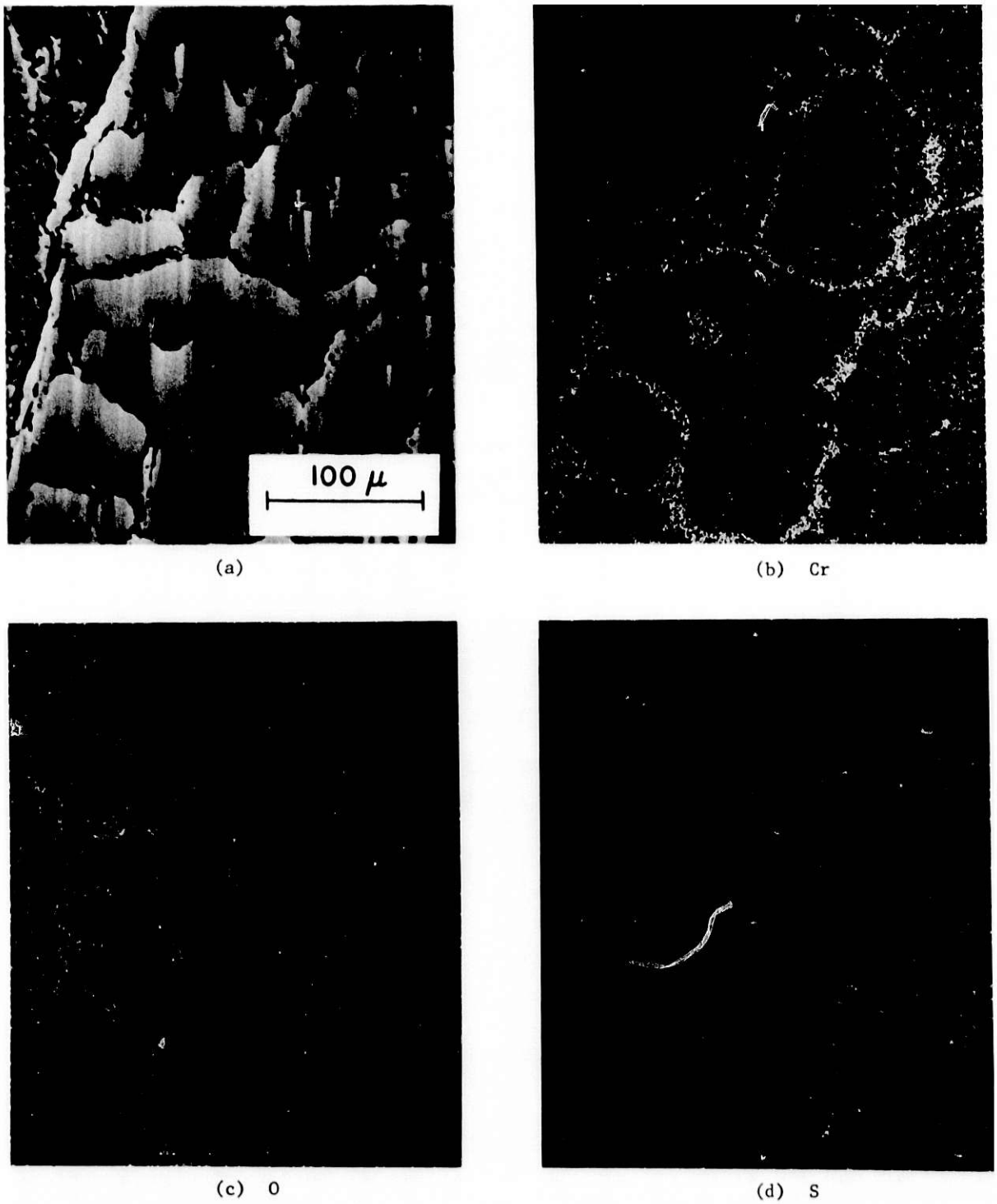

Fig. 28. SEM and Electron Microprobe Analysis of Surface Region Away from Heavily Attacked Area in End Plug from Thermowell 1. The backscattered electron image is shown in (a), and the x-ray maps for selected elements are shown in (b) through (d).

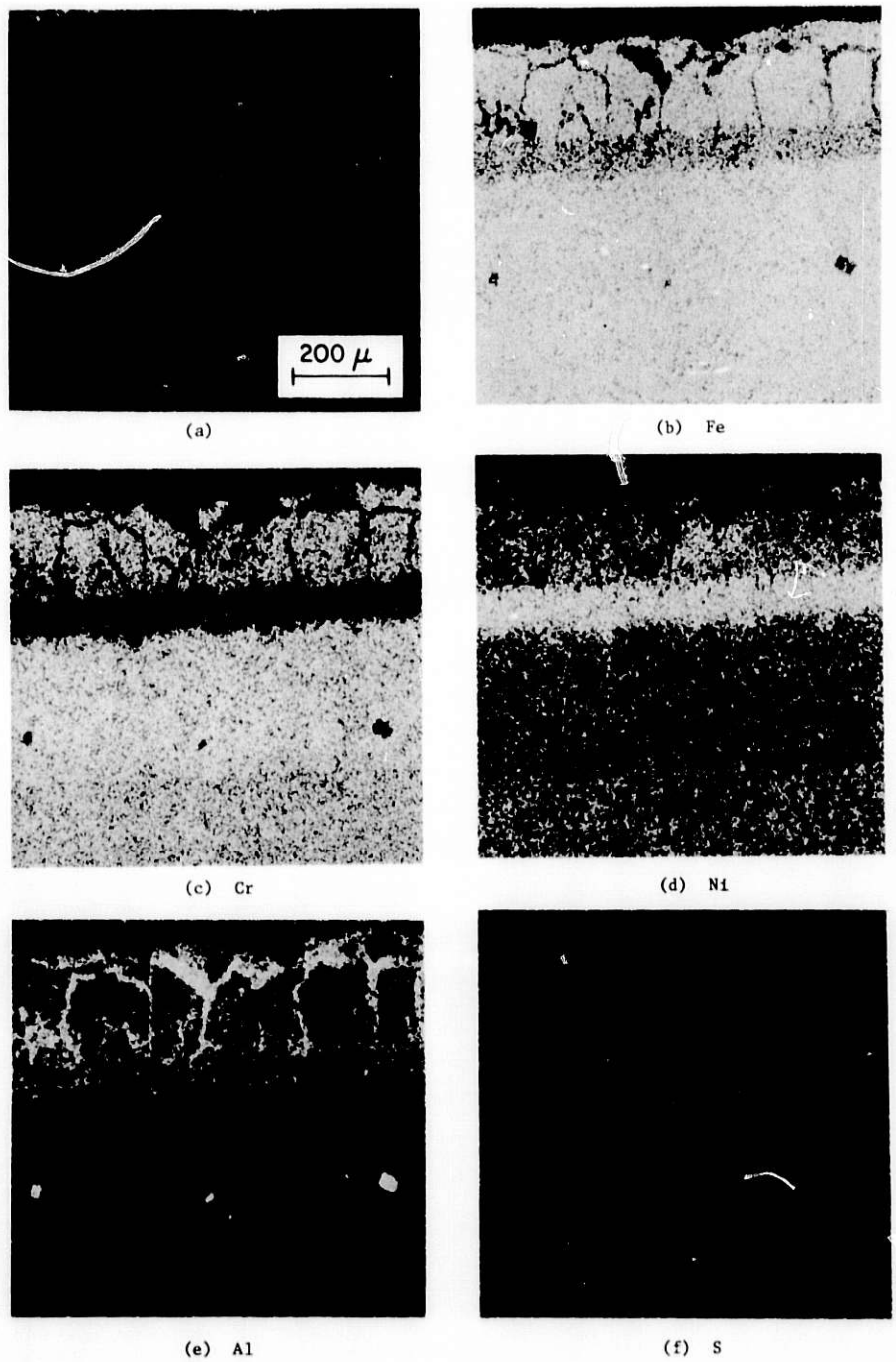

Fig. 29. SEM and Electron Microprobe Analysis of Surface Region Away from Heavily Attacked Region in End Plug from Thermowell 7. The back-scattered electron image is shown in (a), and the x-ray maps for selected elements are shown in (b) through (f).

REFERENCES

1. W.A. Ellingson et al., Materials Technology for Coal-Conversion Processes, Progress Report for April-June 1980, Argonne National Laboratory Report ANL-80-93.

2. A. Muan, Phase Equilibria in the System $FeO-Fe_2O_3-Al_2O_3-SiO_2$, J. Am. Ceram. Soc. 40(12), 429 (1957).

3. W.A. Ellingson et al., Materials Technology for Coal-Conversion Processes, Progress Report for July-September 1980, Argonne National Laboratory Report ANL-80-118.

4. R.E. Beisner, Electromagnetic-Acoustic Transducers: A Survey of the State-of-the-Art, Southwest Research Institute Report NTIAC-76-1 (January 1976).

5. C.F. Vasile, J. Liska and R. Houston, Custom EMAT Instrumentation: Correlation Receiver and Flaw Detector, Proc. ARPA/AFML Review of Progress in Quantitative NDE, AFML-TR-78-205 (January 1979), pp. 52-53.

6. C.M. Fortunko and R.B. Thompson, Application of Electromagnetic Transducers to Nondestructive Evaluation of Welds, Paper Summaries, National Fall Conference of the American Society for Nondestructive Testing, St. Louis, MO, October 1979, pp. 61-66.

7. W. Pardee and R.B. Thompson, EMAT Radiation Patterns, Proc. ARPA/AFML Review of Progress in Quantitative NDE, La Jolla, CA, July 8-13, 1979 (in press).

8. C.M. Fortunko, Weld Inspection with Shear Horizontal Acoustic Waves Generated by EMATs, *ibid.*

9. C.F. Vasile, R.B. Houston and E. Pongraca-Bartha, Portable Instrument for Detecting Surface Flaws using EMATs, *ibid.*

0. R.B. Thompson, R.K. Elsley, W. Petersen and C. Vasile, EMAT Systems for Detecting Flaws in Steam Generator Tubes, *ibid.*

1. J.F. Martin, P.J. Hodgetts, R. Houston, R.B. Thompson and D.O. Thompson, Inspection of Lower Half of Wing Lap Joints with EMATs, *ibid.*

2. K. Natesan, Corrosion and Mechanical Behavior of Materials for Coal Gasification Applications, Argonne National Laboratory Report ANL-80-5 (May 1980).

3. W.A. Ellingson et al., Materials Technology for Coal-Conversion Processes, Progress Report for January-March 1980, Argonne National Laboratory Report ANL-80-46, p. 24.